REVIEW ARTICLE

Scanning electron microscopy with polarization analysis (SEMPA)

M. R. Scheinfein, J. Unguris, M. H. Kelley, D. T. Pierce, and R. J. Celotta
National Institute of Standards and Technology, Gaithersburg, Maryland 20899

(Received 13 November 1989; accepted for publication 27 April 1990)

The high spatial resolution imaging of magnetic microstructure has important ramifications for both fundamental studies of magnetism and the technology surrounding the magnetic recording industry. One technique for imaging surface magnetic microstructure on the 10-nm-length scale is scanning electron microscopy with polarization analysis (SEMPA). This technique employs a scanning electron microscope (SEM) electron optical column to form a medium energy (10–50 keV), small probe (<50 nm) of high current (>1 nA) on a ferromagnetic specimen. Secondary electrons excited in the ferromagnet by the high spatial resolution probe retain their spin-polarization orientation as they leave the sample surface. The spin polarization of the emitted secondary electrons can be related directly to the local magnetization orientation. A surface magnetization map is generated when the spin polarization of the secondary electrons is analyzed as the electron beam is rastered point-by-point across the ferromagnet's surface. In this review article we review the important instrumental components characterizing the SEMPA system. Characteristics of the electron probe forming optics, electron spin-polarization analyzers with associated transport optics, and signal processing electronics will be described. Emphasis on the fundamental design requirements will be stressed. Data acquisition, storage, and processing, as it applies specifically to SEMPA, will be reviewed. Instrumental artifacts specific to SEMPA will be outlined and techniques for their correction given. Examples of magnetic images at high spatial resolution will be shown.

I. INTRODUCTION

The goal of spin-polarized electron microscopy is to describe quantitatively the magnetization distribution in ferromagnetic systems. Since the physical parameters that characterize ferromagnetic systems vary over several orders of magnitude, the resulting magnetic structures in ferromagnets have length scales that vary widely. On large length scales ($>10\,\mu$m), a ferromagnet breaks up into domains in order to minimize its energy. Such domain configurations can only be calculated for the simplest of structures, and in general they are extremely complex and must be determined by observation. The structure of magnetic domains is not only of fundamental interest, but also of considerable technological importance. The size of domains sets a packing limit for high-density magnetic recording media while the sharpness of the domain boundaries limits the signal-to-noise performance. On somewhat finer length scales (>200 nm), the structure of the domain wall that separates domains of different orientation can be seen. Domain walls may be of the Bloch, Néel, asymmetric Bloch, or cross-tie types. All of these domain walls display complicated magnetization distributions, which again, for all but the simplest of cases, cannot be calculated and must be observed. The size of the domain walls may eventually set the ultimate limit on the density of conventional magnetic storage media. Finally, at extremely fine length scales (<50 nm), the structure of magnetic singularities characterized by Bloch lines, Néel caps, and magnetic swirls are seen. These structures may exhibit extremely complex and singular magnetization distributions.

Most methods used for the observation of magnetic microstructure rely on the magnetic fields present in ferromagnetic systems. For example, in the Bitter method[1] fine magnetic particles in solution are placed on the surface where they agglomerate in the fringe fields that are produced at domain walls. The agglomerated particles that decorate the domain walls are imaged using optical techniques. In Lorentz microscopy, the incident electron probe is deflected by the net magnetic field of the sample. In reflection Lorentz microscopy[2,3] bulk magnetic samples may be observed with modest spatial resolution (1000 nm), while in transmission Lorentz microscopy,[3,4] where thin samples are required ($t<300$ nm), very high spatial resolution (10 nm) observation of magnetic microstructure is routine. When the incident electron beam is formed by a scanning transmission electron microscope (STEM) and a subdivided electron detector is used, a differential phase contrast mode of magnetic imaging is possible. These signals yield a Lorentz contrast of extremely high (5 nm) spatial resolution.[5] TEM techniques provide a response averaged over the thickness of the specimen. A constraint on all transmission electron techniques is that samples must be thinned, resulting in magnetization distributions that for most materials do not resemble those of bulk samples. A new technique, magnetic force microscopy (MFM), achieves contrast through the magnetostatic interaction between a ferromagnetic tunneling tip and the fringe fields of the ferromagnet. MFM can be used to locate domain walls and analyze them with high spatial resolution (100 nm).[6] All of these techniques derive image contrast from interactions of the probe with the magnetic fields of the sample and hence offer only an indirect measurement of the sample magnetization distribution. The magneto-optic Kerr effect[7] directly measures the sample magnetization

 0034-6748/90/102501-27$02.00

distribution by determining the rotation of the plane of polarization of light upon reflection. As an optical method, its spatial resolution is diffraction limited to optical wavelengths.

The development of SEMPA resulted from the observation that secondary electrons extracted from ferromagnets have their magnetic moments parallel, and consequently their spins antiparallel, to the magnetization vector at their originating point on the sample.[8,9] This feature is characteristic of transition metal systems as observed in Ni,[10] Fe,[11] Co,[11] and the ferromagnetic glasses.[9] More generally, spin-polarized secondaries may result from excitations by either electrons or photons. Since the polarization of the emitted secondaries is directly proportional to the magnitude and reflects the direction of the net magnetization density for most magnetic systems, a magnetization map is generated by measuring the electron-spin polarization point-by-point across a sample's surface. The principle of scanning electron microscopy with polarization analysis (SEMPA), which in a certain sense constitutes a magnetic spectroscopy, is illustrated schematically in Fig. 1. A finely focused beam of medium energy electrons is used to excite (localized) spin-polarized secondary electrons at the sample surface. The emitted spin-polarized secondaries that carry the signature of the local magnetization of the sample are collected and spin resolved. Magnetization maps can be obtained from the surface of bulk specimens, thin films, and monolayer-type films. The only significant constraints upon the sample is that it be conducting or semiconducting at the surface to prevent charging under the electron beam and that it not have enormous magnetic fringing fields that can depolarize the emitted secondary electrons.

The structure of this review article is as follows. In Sec. II, an overview of the whole SEMPA system will be given. This is followed in Secs. III–VI by detailed descriptions of the individual components that constitute the SEMPA system, the probe forming electron optical column, the spin analyzer, the transport optics, and the signal processing electronics. In Sec. VII, the performance of the entire SEMPA system is summarized with an emphasis on system performance and limitations. Different SEMPA systems in other laboratories are briefly described. Section VIII is devoted to data acquisition and processing. Characteristic examples are used to illustrate system performance and the elimination of instrumental artifacts.

II. SEMPA COMPONENTS: OVERVIEW

The SEMPA technique requires a coupling of diverse and complicated electron-optical components. We will isolate and characterize each of the individual components of the SEMPA system, with an emphasis on the optimization of the complete system.

SEMPA is a surface-sensitive, magnetic microstructural analysis technique. Traditional constraints that apply to conventional surface science analysis instrumentation also apply to SEMPA. The environment local to the specimen must be clean enough to prevent adsorbed gases from coating the surface and diminishing the desired magnetic signals. Since the magnetic contrast is derived from polarized secondary electrons generated near the surface, the magnetic contrast is sensitive to surface electronic structure changes, contamination, and altered work functions, as is the conventional secondary electron intensity contrast.[12] The vacuum requirements are best met in an environment where the pressure does not exceed 1×10^{-9} Torr. Usual ultrahigh vacuum techniques, including all metal seals in the specimen vacuum chamber, are required to prevent contamination of the specimen surface. Conventional surface science preparation (sputter ion gun) and characterization (Auger electron spectrometer) tools should be used to assess the state of the surface. It may be further required to have both heating and cooling capabilities in the sample stage assembly to anneal surfaces and perform temperature-dependent studies or preparations.

A schematic of our SEMPA instrument is shown in Fig. 2. SEMPA is a scanning, focused electron beam experiment.

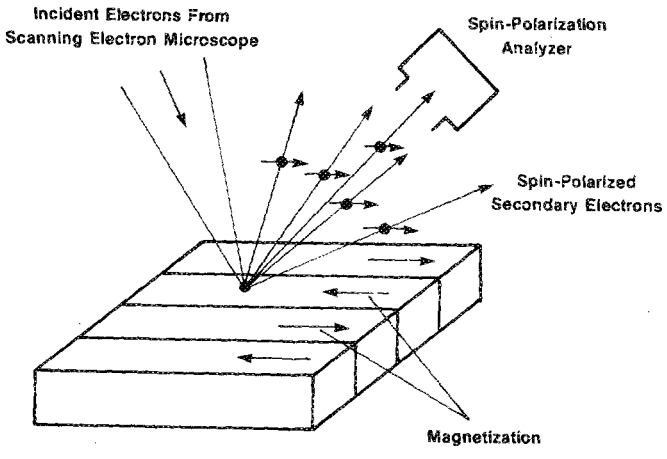

FIG. 1. The principal of SEMPA. A scanned beam of electrons incident on the surface of a ferromagnet creates spin-polarized secondary electrons that are subsequently spin analyzed.

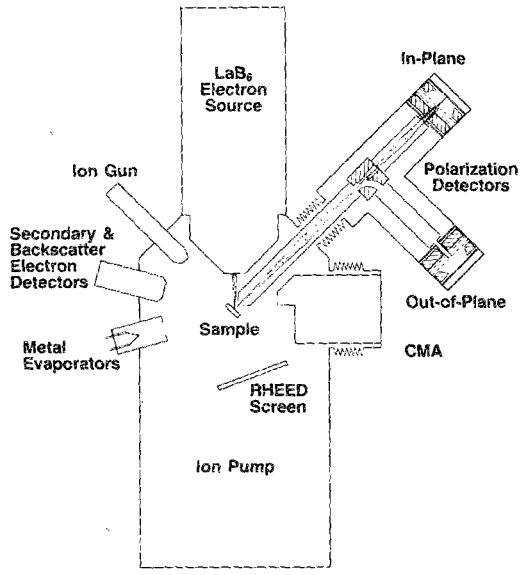

FIG. 2. A cross section of our SEMPA column.

The first critical element of a SEMPA system is the probe forming electron optical column. The probe forming optics have many of the same requirements that conventional scanning electron microscopes (SEMs) and scanning auger microprobes (SAMs) impose on beam energies, currents, and spot sizes. The design specifications for the electron optical column for application to SEMPA will be given in Sec. III.

The second essential component of the SEMPA system is the electron-spin polarization detector. The SEMPA system may be equipped with a single spin detector,[13,14] or multiple spin detectors[15] as shown in Fig. 2. Ideally, two detectors are used for the acquisition of all three orthogonal components of the polarization vector signal. The electron-spin polarization detectors comprise the single most important component of the SEMPA system. It is the inherently inefficient performance of all electron-spin polarization detectors which makes SEMPA both difficult and time consuming compared to the acquisition of conventional secondary electron intensity images. The time necessary to acquire a SEMPA image is typically shorter than the time to acquire an Auger map. As in the past, considerable effort has been exerted toward the improvement of spin detectors. In Sec. IV, a detailed discussion of the spin-polarization detector performance will be given with an emphasis on the adaptability of the detector to SEMPA.

The polarized secondary electrons generated under the focused electron beam must be transported to the spin detectors with a well-defined object-image relationship. We characterize the transport optics to be all the lens elements between the sample in the main chamber and the spin detectors, as schematically indicated in Fig. 2. The transport optics must further extract the secondary electrons as efficiently as possible without introducing any deleterious effects into the focused incident electron beam. This requirement places rather strict limitations on incident beam energies and maximum extraction voltages for the transport optics. Finally, the transport optics must be capable of mapping the scanned spot of the secondary electrons produced under the incident rastered beam, to a position on the spin detector such that undesirable instrumental asymmetries are not introduced. Important design considerations for the transport optics will be given in Sec. V.

The electron probe forming column, spin-polarization detectors, and associated transport optics comprise the essential electron optical components of the SEMPA system. In addition to these components, we characterize the acquisition of magnetic signals using new configurations of particle counting detectors and associated electronics as another critical SEMPA component. We will describe how the signal processing electronics can be implemented in the SEMPA system in Sec. VI.

III. PROBE FORMING ELECTRON OPTICAL COLUMN

The characteristics of the SEMPA probe forming electron optical column, as schematically depicted in Fig. 3, depends upon many important electron optical and mechanical parameters. The important electron optical parameters are the incident beam energy E_0, beam current I_0, probe diameter at the specimen δ, and the probe forming objective

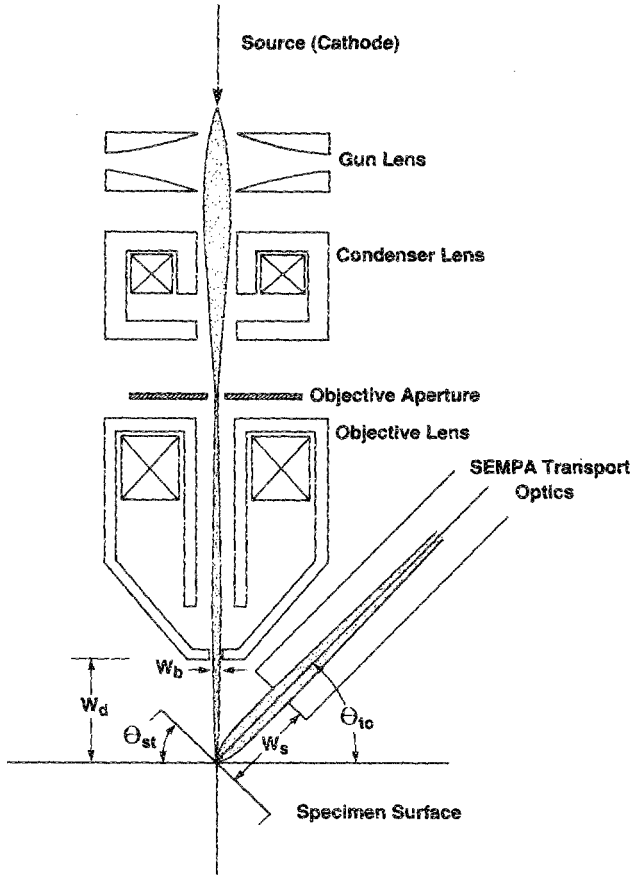

FIG. 3. A cross section of a generic electron optical column illustrating some key design parameters such as the working distance W_d, the exit lens bore W_b, distance of approach of SEMPA extraction optics W_s, stage tilt angle Θ_{st}, and SEMPA transport optics angle Θ_{to}.

lens working distance W_d. The working distance is defined as the distance between the exit pole face of the objective lens and the specimen along the incident beam axis, as shown in Fig. 3. A parameter associated with the electron optical characteristics of the column is the residual magnetic field at the specimen surface. The magnitude of the stray field depends upon the diameter of the exit bore W_b of the objective lens, in the case of magnetic objective lenses, and more generally on the magnetic shielding available for the entire column. Although we have selected magnetic electron lenses for the probe forming optics in our schematic depiction of the column design, all electrostatic lens columns have been realized.[16] These columns have the distinct advantage of reduced magnetic fields at the sample, but in general, it is much more difficult to achieve high current in small probes using only electrostatic lenses. Important mechanical parameters are the maximum stage tilt angle Θ_{st}, the maximum SEMPA extraction optics access angle to the sample Θ_{to}, and the closest approach of the extraction optics to the specimen plane W_s, all shown in Fig. 3. Associated mechanical design considerations are the stage drift, thermal-mechanical stability, and associated acoustic vibrations within the column.

The selection of an incident electron beam energy is the first design compromise. Higher beam energies are employed for higher-resolution probes, but lower beam energies exhibit higher secondary electron yields. In most electron probe forming systems, submicron beam diameters can be obtained for electron energies above 5 keV. The secondary yield decreases rapidly as beam energies are raised. The secondary electron yield from Al, for example, falls from 0.40 at an incident beam energy of 5 keV to 0.05 at 50 keV.[17] Since polarization detectors are of low efficiency, we would like to operate the electron optical column at lower incident beam energies and keep the secondary electron yield as high as possible. The selection of the incident beam energy must also include any effect that the SEMPA extraction/transport optics will have on the incident focused electron beam. The extraction optics must have extraction fields on the order of 100 V/mm to achieve adequate collection efficiency (see Sec. V). Incident beam energies below 10 keV experience deflection aberrations in this extraction field.[18] Thus, we place a lower limit on SEMPA beam energies of 10 keV, the nominal operating point of our instrument.

The current available in the finely focused electron probe depends explicitly on the type of cathode used in the electron gun.[19] Cathodes commonly used in electron probe forming instruments can be classified into two major categories: thermionic emission and field emission cathodes. Newer photoemission cathodes are just beginning to appear as electron sources in probe forming instruments.[20]

Examples of thermionic emitters are the tungsten (hairpin)[19] and lanthanum hexaboride (LaB_6)[19] emitters. These sources are characterized by high emission currents, large solid angles of emission, moderate- to high-energy spreads $\Delta E > 1$ eV, and large electron optical source sizes. Due to the large intrinsic source size of thermionic cathodes, the system demagnification must be on the order of several thousand in order to form a small probe. Thus, thermionic cathodes are good sources for systems where the final probe diameter is relatively large, $\delta > 100$ nm. The current in the final probe decreases very rapidly as the system demagnification is increased making thermionic sources not optimal for use in sub 100-nm spatial resolution systems. The exceptional feature of thermionic cathodes however, is their excellent current stability leading to good noise immunity.

Field emission cathodes[19] can be further classified into two subcatagories: cold field emission and thermally assisted field emission. In field emission, electrons are extracted from the source by applying a large electric field, which reaches a value on the order of 5 V/nm at the surface of the emitting tip. In cold field emission, electrons tunnel through the potential barrier at the surface from the Fermi level inside the metal. Moderate emission currents $I_s = 10\,\mu$A, small energy widths $\Delta E = 0.25$ eV, and extremely small electron optical source sizes $\delta_s = 2$–6 nm are characteristic for these emitters.[21] The system demagnification necessary to employ these sources in high spatial resolution systems need only be on the order of 10, thereby making these emitters the standard in the highest spatial resolution instruments. Unfortunately, the cold field emitters suffer from short-term current instabilities caused by ion backstreaming to the source through the gun.[22]

Thermal field emitters may be operated in the thermal field emission mode or in the Schottky emission mode.[23] These cathodes are characterized by high emission currents $I_s > 0.5$ mA, moderate energy widths $\Delta E > 0.5$ eV, and moderate electron optical source sizes $\delta_s > 8$ nm.[24] The total system demagnification must be about 10. These sources have much more stable emission[22] than cold field emitters, and have much higher emission currents, making them ideal for applications in high spatial resolution spectroscopy experiments.

Electrons extracted from the cathode in the gun are finally focused to a spot on the sample by the objective lens. Magnetic electron lenses have intrinsically lower aberrations than electrostatic electron lenses where the comparison is made for lenses with the same first-order optical properties. This is because the intensity of the magnetic field can be concentrated into extremely small regions of space using high permeability magnetic pole pieces. The intensity of the electric field in electrostatic lens fields is limited by vacuum breakdown. Magnetic lenses most often constitute the probe forming lens of choice. Long focal length magnetic lenses, such as those required in an SEM, are capable of forming moderate to high spatial resolution probes.[25] The ultimate spatial resolution achievable in any electron optical column will be a complex combination of the choice of the cathode, the aberrations of the gun, condenser lens and objective lens, diffraction effects, and space charge beam spreading.[26] In scanning electron microscope columns, the spherical aberration of the probe forming objective lens increases rapidly with increasing working distance. In fact, the spherical aberration coefficient is roughly proportional to the focal length to the third power. Thus, it is desirable to have as short a working distance as possible for optimal probe formation. However, in SEMPA, the polarized secondary electrons must be extracted from the sample surface in a region free from magnetic fields. The design compromise is between longer working distances and smaller probes. Decreasing the working distance decreases the diameter of the probe while increasing the working distance might reduce stray magnetic fields at the sample. Increased working distances are also desirable since space is required to extract the polarized secondary electrons. Another design compromise in the selection of an objective lens involves the choice of the exit bore of the lens W_b. One minimizes the stray field by decreasing the exit lens bore at the expense of decreasing the maximum scan range.

In Fig. 3, the SEMPA access (maximum) angle Θ_{to} is shown. This angle is the maximum angle that the SEMPA extraction optics makes with a plane perpendicular to the incident electron beam direction. This angle will be limited by the objective lens working distance W_b and the geometrical shape of the objective lens pole piece.[25] It is desirable in SEMPA to have the plane of the specimen parallel to the plane of the spin-polarization detectors. If this criteria is to be met, the specimen tilt angle $\Theta_{st} = 90° - \Theta_{to}$. The larger the specimen tilt angle Θ_{st}, the larger the probe is at the sample in the direction of the tilted plane, that is, as the stage is tilted, the probe becomes elliptically elongated along the tilt direction. To minimize this probe elongation along the tilt direction, it is desirable to minimize Θ_{st}. Clearly, as Θ_{st} is

minimized, Θ_{to} increases until the SEMPA extraction optics interferes with the objective lens pole piece. Optimally, Θ_{st} should be as small as possible, but for most objective lens shapes, and typical working distances necessary to extract the polarized secondary electrons, $\Theta_{st} \approx 45° \approx \Theta_{to}$. This results in a probe-size elongation in the tilt direction of $\sqrt{2}$.

The spatial resolution of SEMPA will be limited by the long-term stability of all of the components over the time necessary for the acquisition of a magnetic image. For long acquisition times, the mechanical stability of the stage will ultimately be the limiting factor in determining the spatial resolution. For experiments where the specimen must be heated or cooled, the thermal-mechanical stability of the sample/stage assembly can critically limit the final spatial resolution.

The ultimate spatial resolution in the SEMPA magnetic images depends critically upon the performance of the electron probe forming column. The lateral spatial resolution necessary for any particular set of experiments depends upon the length scales of the magnetic properties being investigated. For reasonable SEMPA acquisition times, a topic that will be addressed in Sec. VII, incident beam currents of at least 1 nA are necessary (we assume nominal values of the secondary electron yield to be 0.25–0.40). With the further constraint that the working distance of the objective lens be at least 10 mm, we conclude that field emission sources are best suited for investigations in the range below 100 nm and thermionic sources such as LaB_6 provides sufficient current for probe sizes above 100 nm.

What is the correlation between the spatial resolution that is expected in SEMPA images with the beam diameter in SEM? The energy deposited into bulk samples is characterized by the well known "blooming" phenomenon whereby the beam expands greatly in the bulk due to multiple scattering.[17] Does this degrade the spatial resolution in SEMPA? The escape depth of true polarized secondary electrons has been calculated to be on the order of nanometers.[27] As in conventional SEM, the resolution of the magnetic signal obtained from polarized secondaries excited by SEM probes should be that of the focused beam, for beam diameters in excess of about 10 nm. For nm scale beams, the ultimate resolution can be estimated by a combination of the incident beam profile and the spatial distribution of the secondary electrons generated from multiple scattered electrons that are close enough to the surface to escape.[28] In general, long focal length objectives are not capable of forming nm scale probes without immersing the sample in the field of the objective lens. For our purposes, the lateral spatial resolution of SEMPA will be defined as the probe diameter at the sample surface.

IV. SPIN-POLARIZATION DETECTORS

A. Analyzer performance

The electron spin-polarization analyzer is central to the SEMPA experiment. Although there has been considerable progress in reducing the size and increasing the efficiency of spin detectors, the fact remains that spin detectors are terribly inefficient. For example, the measurement of a beam polarization comprised of N_0 electrons is $P_0 \pm \delta P$, where the uncertainty or relative error of the measurement is $\delta P = 1/(N_0 F)^{1/2}$. F is the figure of merit for a spin-polarization analyzer and will be discussed below. The figure of merit for the highest-performance spin detectors rarely exceeds 1×10^{-4}. In the case of the measurement of the polarization of a beam comprised of N_0 electrons, the relative uncertainty of the beam polarization is $\delta P/P_0 = 1/(P_0^2 N_0 F)^{1/2}$, while the relative uncertainty in the intensity measurement is $\delta N/N_0 = 1/(N_0)^{1/2}$. Comparing these expressions, we can see that it takes at least 10^4 times as long to acquire a polarization measurement as an intensity measurement with the same statistics! This places SEMPA intermediate between SEM and Auger imaging in signal acquisition time.

The spin-dependent interaction which is the basis of most electron-spin detectors is the spin-orbit interaction. When an electron of spin $\mathbf{s}$ scatters from the central potential $V(\mathbf{r})$ of some high Z element, there is an additional term in the interaction Hamiltonian that results from interaction of the electron spin $\mathbf{s}$ with its orbital angular momentum $\mathbf{L}$ in the central potential field.[29] The spin-orbit interaction has the effect of making the cross section larger or smaller for electrons with spin parallel or antiparallel to the normal $\mathbf{n}$ to the detector scattering plane. This is referred to as Mott scattering as contrasted to Rutherford scattering where the spin-dependence of the scattering is not included. The scattering plane is defined as that plane in which both the incident and scattered electron trajectories lie. The normal to the scattering plane $\mathbf{n}$ is defined in terms of the incident wave-vector $\mathbf{k}_i$ and the scattered wave-vector $\mathbf{k}_f$ as follows:

$$\mathbf{n} = (\mathbf{k}_i \times \mathbf{k}_f)/|\mathbf{k}_i \times \mathbf{k}_f|. \tag{1}$$

The cross section for the scattering can be written[29]

$$\sigma(\Theta) = I(\Theta)[1 + S(\Theta)\mathbf{P}\cdot\mathbf{n}], \tag{2}$$

where $\mathbf{P}$ is the beam polarization, $\mathbf{n}$ the normal to the scattering plane, $I(\Theta)$ the angular distribution of backscattered current, and $S(\Theta)$ is the Sherman function for the detector scattering material. The Sherman function is a measure of the strength of the spin-dependent scattering, and is in general a complicated function of beam energy and angle.[30,31] In order to determine the polarization of the beam, one measures a spatial asymmetry A between the number of electrons scattered to the "left" N_L and the number to the "right" N_R. The left and right detectors are defined relative to the incident beam direction and the normal to the scattering plane $\mathbf{n}$. The "up-spin" direction is defined to be parallel to $\mathbf{n}$, and the "down-spin" direction is antiparallel to $\mathbf{n}$. The measured scattering asymmetry A is

$$A = (N_L - N_R)/(N_L + N_R) = PS, \tag{3}$$

which is directly related to the beam polarization by $A = PS$, where S is the integrated Sherman function for the entire range of angles collected.

The figure of merit F for a spin-polarization detector is defined as[29]

$$F = S^2 I/I_d, \tag{4}$$

where I is the backscattered current intensity collected at the electron counters and I_d is the incident beam intensity. The figure of merit is characteristic of the counting statistics of a

polarization experiment and is useful for comparing different spin-polarization detectors.

Systematic errors also contribute to the uncertainty in spin detectors. There are several types of instrumental asymmetries. Since the measurements are based upon a left/right scattering asymmetry, any instrumental asymmetry in the detector introduces an offset into the measurement. These asymmetries may be the result of unequal gains in the left and right channels of the signal processing electronics, unequal sensitivities of the electron multipliers, and mechanical imperfections that result in a detector geometry that is not symmetric. Other instrumental asymmetries may be introduced by motion of the incident beam. Uncontrolled apparatus asymmetries of this type, such as changes in the position or angle of the incident electron beam on the scattering target in the detector, are undesirable. Care should be taken to minimize these disturbances by designing the coupling electron optics to produce minimal instrumental asymmetries.

One of the main differences in spin analyzers is that the incident beam energy for scattering within different detectors may vary over three orders of magnitude from around 100 eV to 100 keV. The most obvious implication of this observation is that we might expect that the physical size of the detectors will vary greatly, which is indeed the case. Low-energy spin detectors can be made far more compact than their high-energy counterparts. However, in low-energy scattering detectors, surface cleanliness of the scattering target is extremely important, while high-energy detectors are relatively insensitive to the surface of the scattering target in the detector. We will now review the properties and operation of the more common spin detectors and then discuss the differences which are important for application to SEMPA.

A Mott analyzer is a device for measuring the spin component transverse to the scattering target in the detector by utilizing the left-right asymmetry of the spin-dependent Mott scattering of electrons at high energies from high atomic number targets. Until recently, Mott analyzers had cylindrical symmetry, operated at incident energies of 100–200 keV, and detected the asymmetry at scattering angles around 120° (to the incident beam direction).[29,32,33] The Sherman function $S(\Theta)$ is a function of the scattering angle for high-energy Mott scattering and is a maximum near 120°.[34] The detector efficiency is maximized by collecting scattered electrons over the angular range of $120° \pm 20°$ where the Sherman function is still large. An alternative to the classical Mott design has been constructed using spherical symmetry in order to minimize instrumental asymmetries.[35] Although these Mott detectors have high Sherman functions and reasonably high figures of merit, they are physically large and bulky, and require high voltages. Their large size makes them particularly difficult to adapt to SEMPA.

Lower-energy Mott analyzers and retarding Mott analyzers have been realized in a number of new spin polarimeters.[36–41] In this case, an electron beam is accelerated in a radial field between an outer electrode at nearly 1 keV potential to 20–30 keV by an inner electrode. It scatters from a target and is then decelerated by the same radial field before striking a detector at the lower potential. They have reduced size when compared to the traditional Mott analyzers. The electrons are once again collected at angles around 120° to the incident beam. The retarding field present in these detectors helps discriminate against inelastically scattered electrons to prevent them from reaching the electron counters. Retarding Mott analyzers have been realized in spherical[36] and cylindrical geometries.[38–41] A salient feature of retarding Mott analyzers is that the electron detectors (counters) are at low voltage and the vacuum housing is at ground potential making them much more convenient than traditional Mott detectors. However, high voltages are still required and their physical size is still sufficiently large that interfacing with an electron microscope column is difficult. Further, the retarding fields greatly limit their efficiency.

The analyzers discussed above operated in an energy range higher than 20 keV. The low-energy electron diffraction (LEED) electron-spin polarization detector, in contrast, operates at about 100 eV.[42–45] In this detector the diffraction from a single crystal target, usually *W*, is exploited by detecting the spin asymmetry of scattered electrons concentrated in the diffracted beams from the target's surface. The collimating properties of diffraction by a single crystal make this a very efficient spin analyzer. This detector can be quite small due to the low energy of the scattering. Furthermore, this detector has a high Sherman function and figure of merit, but suffers from sensitivity to incident beam angular deviations. The constraints on the incident beam angular spread ($< 2°$) and energy spread (< 5 eV) are severe but are not an insurmountable problem for application to SEMPA. The main drawbacks of this detector are the requirements that the crystal target be flash cleaned at high temperatures (> 2000 K) every quarter hour, and that it be maintained in a 1×10^{-10} Torr vacuum which may be incompatible with the electron microscope chamber.

Another low-energy electron-spin polarization detector is the absorbed current detector.[46–49] The absorbed current detector may be the cheapest and simplest of all spin polarimeters. The spin dependence of the absorbed current results primarily from the spin dependence of elastic scattering. When electrons of one spin orientation are preferentially scattered, electrons of the other spin orientation are preferentially absorbed. The absorbed current detector operates at a beam energy where the unpolarized secondary electron yield is one, that is, where the number of electrons leaving the sample and incident upon the sample are equal, leaving zero absorbed current. Spin-dependent absorbed currents are measured relative to this operating point by detecting negative currents for one spin orientation and positive currents for the other spin orientation. This detector has a high figure of merit, but it is extremely sensitive to the incident beam angles onto the surface of the scatterer in the detector. Furthermore, because it cannot be used in a pulse counting mode, it is extremely difficult to measure small currents at high bandwidths as required in SEMPA.

The last electron-spin detector that we consider is the low-energy diffuse scattering (LEDS) detector.[50–53] Like the LEED and absorbed current detectors, it operates at low energies of about 150 eV. It employs an evaporated polycrys-

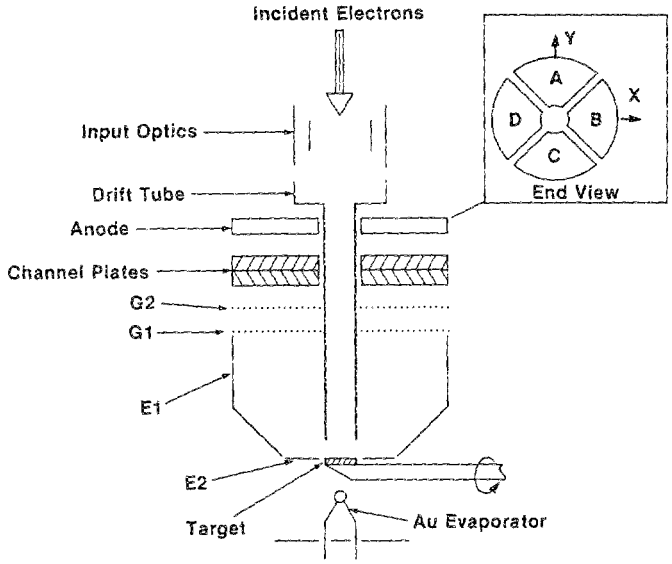

FIG. 4. A cross section of the LEDS detector. The divided anode assembly is shown in the inset as viewed from the Au target.

talline Au target, which is stable and remains clean for a number of days in a 1×10^{-9} Torr vacuum. The polycrystalline film diffusely scatters the incident electrons. The efficiency of this detector is increased by collecting the scattered electrons over large solid angles. This results in the highest figure of merit of any spin-polarization detector.[52] The detector is compact, movable, and in general well suited to a number of experiments including SEMPA.

Since the low-energy diffuse scattering polarimeter is the detector of choice for our SEMPA apparatus, we include a schematic cross section in Fig. 4 and will briefly describe its operation.[50,52] We will use it as an example to motivate the discussion on instrumental asymmetries. In the LEDS detector, electrons of 150-eV kinetic energy are incident upon the evaporated Au scattering target. The Au target, the electrode coplanar with the target E_2 and the input drift tube are all at the beam potential such that the electrons enter into the detector in a field-free region. The input optics are used to achieve the desired beam focus on the Au foil. The electrons are backscattered from the Au target diffusely. The angular dependence of the elastic scattering, including the elastic spin asymmetry scattering has been calculated by Fink and co-workers.[30,31] Owing to the nearly isotropic angular distribution of the emitted electrons, the focusing electrode E_1 is negatively biased by -125 V relative to the Au foil. This deflects the electrons such that their trajectories are normal to the grids G_1 and G_2. The energy selectivity of the retarding grid G_2 is thereby greatly enhanced and both the Sherman function and the collection efficiency are increased. G_1 can be held at the incident beam potential (energy) or at a slightly positive ($+75$ V) bias with respect to the Au foil.[52] Positive G_1 helps keep the electrons' trajectory normal to the grids. G_2 is the energy selecting electrode. This grid is nominally negatively biased by -30 to -50 V with respect to the Au target such that no true secondaries created at the Au target reach the channel plates. Once the electrons pass through G_2, they are multiplied by channel plate electron multipliers and detected by a high voltage anode which is divided into four sections. Each anode subsection subtends an azimuthal angle of 90° as indicated in the inset of Fig. 4. Two orthogonal components of the polarization vector may be measured simultaneously with this detector as,

$$P_x = 1/S(N_C - N_A)/(N_C + N_A), \tag{5}$$

$$P_y = 1/S(N_B - N_D)/(N_B + N_D), \tag{6}$$

where N_i is the number of electrons counted by quadrant "i." This detector achieves its high performance by having a very high collection efficiency I/I_d, obtained by collecting the scattered electrons over very large solid angles. The performance is further enhanced by carefully selecting the cutoff energy for the scattering from the Au target by insuring that the scattered electron trajectories are nominally perpendicular to the grids. Optimum selection of the minimum and maximum scattering angles subtended by the grids is fixed by the entrance drift tube and E_1.

The important parameters of the various polarization detectors are summarized in Table I. We include in Table I a comparison of the detector incident electron energy E_d, detector Sherman function S, the fraction of collected current I/I_d, the figure of merit F, the detector's physical size, and the vacuum requirements. The figure of merit is applicable for spin-polarization experiments where the uncertainty is determined by counting statistics. It is also desirable to have a detector with a high Sherman function to minimize the effects of instrumental asymmetries. The absolute value of the detector Sherman function of spin polarimeters are all calibrated against the traditional Mott detector which in turn is usually calibrated against theoretical values.[33,51,54,55] For application to SEMPA, it is extremely important that

TABLE I. Comparison of the performance of the different polarimeters.

Analyzer	E_d (keV)	S	I/I_d ($\times10^{-3}$)	F ($\times10^{-4}$)	Size (m^{-3})	Vacuum (Torr)	Reference
Mott	100	-0.26	1.5	1.0	10	1×10^{-5}	32
Ret. Mott	30	-0.17	7.0	0.2	0.1	1×10^{-5}	38
LEED	0.105	-0.27	2.2	1.6	0.001	1×10^{-10}	44
Abs. curr.	0.162	[a]	[a]	1.0	0.001	1×10^{-9}	48
LEDS	0.150	-0.10	10	1.0	0.001	1×10^{-9}	50
LEDS	0.150	-0.11	20	2.0	0.001	1×10^{-9}	52

[a] Parameters not strictly defined for this detector. See Ref. 48.

the detector be small. When the detector is interfaced to the electron optical column, it must not mechanically destabilize the column itself. Finally, it is desirable that the detector's vacuum requirements be compatible with those of the specimen chamber in the electron optical column for easy interfacing.

B. Instrumental asymmetries

Instrumental asymmetries can be caused by nonuniformities in the spin detector. Any geometrical asymmetry or a variation in the gain in the electronics in the signal channels can manifest itself as an error in the polarization measurement. This is a consequence of the fact that the detectors rely on a left/right scattering asymmetry in order to measure the polarization of an electron beam. All of the detectors are sensitive to the position and angle of the beam at the detectors. Owing to imperfections in mechanical alignment, or if precise beam alignment and control during an experiment cannot be guaranteed, an instrumental or false asymmetry may occur. Any effect that introduces spurious signals systematically into either the left or right scattering channels introduces a false asymmetry.[52,54,56] Another cause of instrumental asymmetry results from the actual movement in position or angle of the incident beam. Such beam movement is characteristic of many spin-polarized electron experiments such as SEMPA and spin-polarized photoemission. Any of these effects contribute to the total systematic instrumental asymmetry A_I. In order to characterize A_I, we must determine the total number of electrons reaching the left and the right scattering channel of the detector for a given beam alignment condition.

A schematic cross section of a "generic" polarization detector based on the principles described above is shown in Fig. 5(a). A detector consists of a left and a right channel, labeled L and R (relative to the incident beam direction). There are two detectors shown in the figure, differing only in an overall size, where the first detector, labeled "1," consisting of L and R channels, is in close proximity to the Au foil, and the second detector "2," also consisting of L and R channels, is further from the Au foil. Assume that the out-of-plane angles are identical to the in-plane angles; in other words, the electron detector cross section could be that of a conventional Mott analyzer with circular acceptance apertures into the L and R electron counters. As indicated, both of the detectors subtend the same solid angle at the Au target, and thus both detectors have the same collection efficiency and must therefore have the same figure of merit. Further, both of the detectors have the same average scattering angle from the central axis of the detector, denoted by Θ_0, and the same inner and outer limits on the scattering angles, Θ_{in} and Θ_{out} The coordinates of the intersection of the axis of each channel with the detector planes for the two detectors are different, and are denoted by $\bar{x}_1$, $\bar{x}_2$, $\bar{z}_1$, and $\bar{z}_2$.

For an unpolarized incident electron beam, the number of electrons collected in channels L and R is given by

$$I_i = \int_{\text{det}} \frac{d\sigma(\Theta,\Phi)}{d\Omega}\, d\Omega_i, \tag{7}$$

where I_i is the current measured by a signal channel,

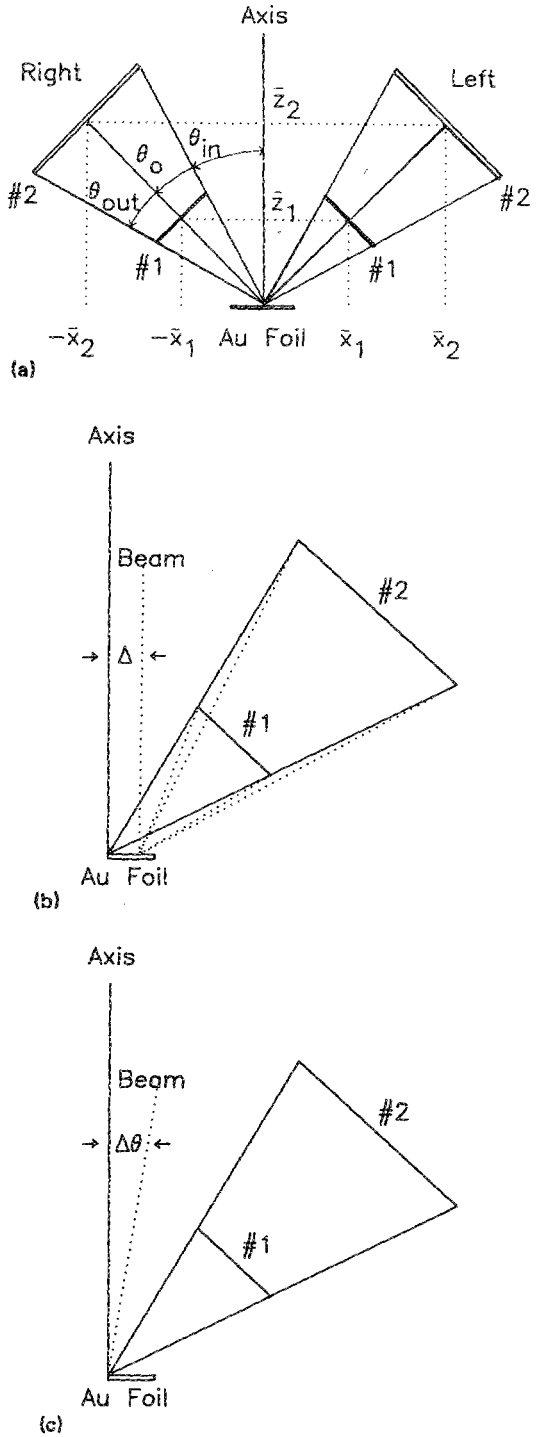

FIG. 5. (a) A cross section of a generic spin analyzer that determines polarization by left/right scattering asymmetry. Two separate detectors are shown, a small detector "1" and a larger detector "2." (b) Displacement asymmetry and (c) angular asymmetry resulting from poorly controlled beams.

$d\sigma(\Theta,\Phi)/d\Omega$ is the differential cross section for the scattering process, and Ω_i is the solid angle subtended by a signal channel. The instrumental asymmetry A_I associated with this configuration is

$$A_I = (I_L - I_R)/(I_L + I_R). \tag{8}$$

If the beam moves or tilts on the scattering target, an instru-

TABLE II. Comparison of detector instrumental asymmetries for various polarimeters.

Analyzer	Reference	$\bar{x}$ (mm)	$\bar{z}$ (mm)	θ_0	θ_{in}	θ_{out}	A_{Id} (%/mm)	$A_{I\Theta}$ (%/deg)
Mott	35	26.7	13.6	63°	43°	83°	6.1	2.0
Ret. Mott	36	29.4	17.0	60°	54°	66°	5.5	2.0
Ret. Mott	38	14.0	8.5	59°	49°	69°	13.9	2.1
LEDS	50	3.7	3.7	45°	30°	60°	28.0	6.0
LEDS	52	12.8	11.2	49°	30°	68°	6.0	6.0

mental asymmetry A_I will result from changes in the solid angle Ω and changes in the relative cross section $\sigma_i(\Theta,\Phi)$ subtended by each channel. We consider these effects for the two detectors proposed in Fig. 5(a).

Figure 5(b) depicts a pure displacement Δ of the beam at the Au foil. It is clear now that the two detectors are no longer identical. Without considering the relative change in the cross section for the two detectors, it is evident that detector 1, the smaller of the two, suffers from the larger instrumental asymmetry. As the beam moves towards one channel of the detector, as in this case towards the R channel, that channel receives more electrons due to the incremental solid angle subtended; the other channel, the L one in this case, receives less, yielding a negative displacement instrumental asymmetry A_{Id}. It seems that the requirement that the spin-polarization detector be small for application to SEMPA contradicts the need for the detector to be large to minimize beam displacement instrumental asymmetries. This is a design issue of extreme importance, for we seek to keep the physical size of the detector small while we wish to have the detector's electron optical size to be large in order to decrease its sensitivity to instrumental asymmetries.

Figure 5(c) depicts a pure angular deviation $\Delta\Theta$ of the incident electron beam. As can be seen, there is no change in solid angle due to a pure tilt. However, when the angular dependence of the cross section is taken into account, an angular instrumental asymmetry, $A_{I\Theta}$, results. The cross section has a functional Θ dependence that exhibits a strong enhancement in the backscattered direction.

Spin-polarization analyzers appear to have non-negligible instrumental asymmetries as summarized in Table II.[52] Careful electron optical design is required to further reduce this deleterious effect as detector sizes decrease.

Consider the schematic depiction of a detector and the ray paths in Fig. 6. This is a generic spin-polarization detector. The incident electron ray paths are shown off-axis and tilted. The ray is displaced towards the R channel, yet it is tilted toward the L channel. Qualitatively, in this regime, the R channel receives more electrons due to the displacement and the enhanced solid angle, but yet it receives fewer electrons due to the tilt and the decrease in $d\sigma(\Theta)/d\Theta$. Similarly, the L channel receives more electrons due to the tilt, yet fewer due to the displacement. If the asymmetry due to displacement can exactly balance that asymmetry due to angle for a given set of input conditions, then the total instrumental asymmetry A_I can be markedly reduced. To meet these conditions, the following criteria must be met[29,52,54,56]:

$$f(\Delta\Theta) = \int_{\text{det}} \frac{d\sigma(\Theta,\Phi)}{d\Omega}\, d\Omega_i\,, \tag{9}$$

$$g(\Delta) = \int_{\text{det}} \frac{d\sigma(\Theta,\Phi)}{d\Omega}\, d\Omega_i\,. \tag{10}$$

The integral of the cross section over the detector must be a function of the misalignment angle $\Delta\Theta$, and the integral of the cross section over the detector must also be a function of the displacement misalignment Δ. What is essential for compensation is that the angular and displacement asymmetries are equal and opposite. We find that the functional dependence of both integrals is quasilinear. Since the asymmetries are quasilinear in displacement and angles, we can balance them against each other using the first-order real imaging properties of electron lenses on the input to the detector. Note that the displacement misalignment integral is dominated by changes in the solid angle. If these (linear) relationships can be satisfied, then a set of (linear) equations in misalignment angle $\Delta\Theta$ and misalignment displacement Δ can be solved to yield zero instrumental asymmetry for known detector displacement and angular asymmetries. This is driven by the fact that most physical designs automatically constrain the likely displacements and enforce some kind of correlation between the displacements and angles at the detector target foil. We wish to exploit this correlation when we discuss the role of the transport optics and propose some solutions to the instrumental asymmetry problem for the SEMPA experiment.

It is instructive to compare once again the relative merits of the various detectors presented in light of the discussion on asymmetry. The obvious advantage to a high-energy polarimeter is that the electron optical properties of these

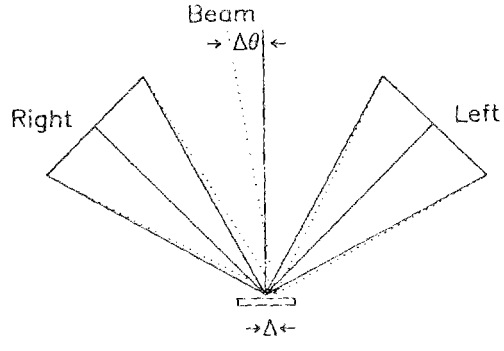

FIG. 6. Instrumental asymmetry compensation scheme whereby angular and displacement asymmetries cancel each other.

systems tend to be, although not always, less sensitive to misalignment asymmetries. This is a direct consequence of operating at higher beam energies. However, these systems are necessarily larger and can introduce mechanically destabilizing effects into the probe forming electron optical column.

V. TRANSPORT OPTICS

The purpose of the transport optics is twofold. Primarily, the transport optics must efficiently extract, collect, and transfer the spin-polarized secondary electrons from the specimen surface to the spin-polarization detectors. Second, the transport optics must map the scanned spot under the electron beam on the specimen surface, which serves as a source of polarized electrons, to a place on the detector scattering target such that instrumental asymmetries are minimized.

Some general concepts involving phase space allow us to describe the collection and transfer aspect of the transport optics most precisely. For macroscopic electric and magnetic fields, the conservation law of Helmholtz–Lagrange (e.g., Refs. 57 and 58) states that, for any two points along a beam path, the product of the beam's energy E, cross-sectional area A, and solid angle Ω are constant. The subscripts "s" and "d" denote the sample and detector planes, respectively:

$$dE_s\, dA_s\, d\Omega_s = dE_d\, dA_d\, d\Omega_d. \tag{11}$$

The design problem of the transport optics in the SEMPA system is to map the phase space at the specimen surface to the detector. The phase space at the sample surface is approximated by multiplying $E_s = 4\ \text{eV} \pm 4\ \text{eV}$, $A_s = \pi\delta^2/4$, where δ is the incident beam probe diameter and $\Omega_s = 2\pi(1 - \cos\Theta_s)$. Θ_s is the maximum take-off angle of secondaries, as measured from the sample normal, allowed into the entrance aperture of the extraction electrodes.

For the LEDS detector, for example, we have determined that the instrumental asymmetry is $A_{Id} = 6\%/\text{mm}$. For the same detector, with a detector Sherman function of $S = 0.10$, the measured polarization will vary by $P = A_{Id}/S = 60\%/\text{mm}$. If the absolute measurement of the polarization due to instrumental asymmetry has to be on the average about 0.5%, we find that the maximum displacement of the beam on the detector must be smaller than $10\,\mu\text{m}$. We take this to define an upper limit on the illumination area of the detector, A_d. Since the convergence angle of the beam incident on the Au target is fixed to be less than 2° (homogeneously distributed about the electron optical axis such that the net angular instrumental asymmetry is zero), and the beam energy of the detector is $E_d = 150\ \text{eV}$, the product $E_d\, A_d\, \Omega_d = 22\ \text{eV}\,\mu\text{m}^2\,\text{sr}$. If this is matched at the input to the transport optics, and nominally $E_s = 4$ eV and A_s $7.85\times10^{-3}\,\mu\text{m}^2$ (characteristic of a 100-nm-diam probe), then the maximum acceptance solid angle into the entrance of the transport optics can be $\Omega_s = 2\pi$. This means that one should "ideally" be able to collect all of the electrons and transfer them to the detector for the fixed beam case and achieve the desired polarization resolution. We will deal with the issues of a scanned beam shortly.

In order to determine the efficiency with which electrons can be extracted from the sample surface it is necessary to consider the sample (the cathode) and the first electrode of the transport optics (the extraction electrode) as the electron optical equivalent of a gun. Essentially, the sample is part of the transport optics, and, as such, the sample and stage should be as flat and uniform as possible.

In Fig. 7, an idealization of the extraction region near the sample is shown. Ideally, the sample and the front plate of the extraction electrode should be parallel for the simplest beam extraction control. Noncoplanar configurations do exist, but the analysis and beam control is more complicated.[59] The equations of motion for a secondary electron emitted from the sample surface at an energy E_s corresponding to a potential V_s, at an angle from the sample normal Θ_s can be solved analytically. The maximum distance from the axis $r_{\max}$ that the particle can lie at the extraction electrode plane at a potential V, and can still be collected is given by

$$r_{\max} = \frac{2W_s V_s}{V}\sin\Theta_s\left[\cos\Theta_s\left(\cos^2\Theta_s + \frac{V}{V_s}\right)^{1/2}\right]. \tag{12}$$

The angle Θ_f that the electron makes at the extraction electrode plane is given approximately by

$$\tan\Theta_f = \sin\Theta_s/(\cos^2\Theta_s + V/V_s)^{1/2}. \tag{13}$$

The effective object for the transport optics, shown in Fig. 7, is determined from the intercept of the asymptotic ray trajectory at the extraction electrode with the optic axis. The virtual object position is a critical parameter for the correct design of the electron optics.

In order to determine the relative size of the extraction fields, we must look at the requirements that limit the size of the transport optics lens elements. As determined in Sec. III, the working distance of the lens is about 10 mm, the stage is tilted by 45° to the incident electron beam, and the extraction electrode for the transport optics is likely to be no closer than 10 mm to the sample surface. Given these constraints, we determine that the size of the transport optics at the extraction electrode should have a maximum inner diameter of about 10 mm. The acceptance aperture should be on the order of 2.5 mm in diameter, perhaps even smaller. For a 2.5-mm-diam entrance aperture, the differential angular collec-

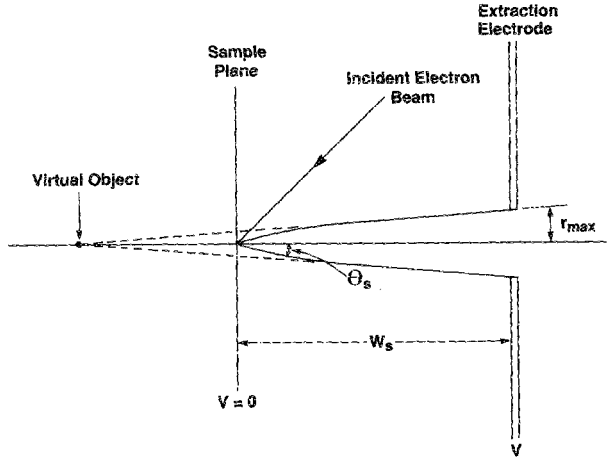

FIG. 7. Schematic of electron optics of extraction region near the sample.

tion efficiency $d\eta_{exa}/dE_s$ can be determined as a function of the incident beam energy and extraction potential as given in Table III. The secondary electron angular emission distribution is assumed to be cosine like Ref. 17. The total angular collection efficiency η_{exa} is the integral of the differential angular collection efficiency weighted by the fraction of secondary electrons emitted in that energy interval. The total collection efficiency of the transport optics η_{ex} is a product of the angular collection efficiency η_{exa} and the energy collection efficiency η_{exe}. The energy collection efficiency can be determined from a model secondary electron energy distribution,[17] which can then be integrated over the energy window of the detector to determine the fraction of secondaries collected. We select the nominal energy value for the peak in the secondary electron energy distribution to be 4 eV. The fraction of electrons in a specified energy window is approximated in Table IV.

In order to achieve the highest possible efficiency for all true secondaries, for the limited design criteria given above, the energy window should be 4.0 ± 4.0 eV and the extraction potential should be 500 to 1000 V or larger. The total angular efficiency is obtained by weighting each element in a column of Table III by the secondary electron energy distribution function. This requirement of a large collection efficiency demands a large extraction field. The 1000-V extraction field was used in Sec. III to place a lower limit on the incident beam energy in the electron optical column.

Once the electrons have been extracted from the sample, the virtual object point is the new source, or the object for the transport optics. The image must now be mapped onto the detector plane. Polarization detectors only measure components of the spin in the plane of the scattering target in the detector. When all three components of the vector polarization must be measured, the transport optics must be capable of distributing the beam to either of two perpendicularly oriented detectors, as shown in Fig. 2. An alternative technique for the measurement of all three components of the polarization vector is the use of a spin rotator[60–64] and only one polarization detector. Although both of these options are viable, we will emphasize the design constraints in the present system. We utilize a quarter-sphere[65,66] "switchyard" to deflect the electron beam onto the "right-angle" detector, without rotating the spins in order to measure the component of the spin polarization out of the plane of the sample. The principal of spin rotation is reviewed in Refs. 60–64 and will not be explained here.

TABLE III. Differential angular collection efficiency vs extraction electrode potential.

Energy (eV)	$d\eta_{exa}/dE_s$ in (%) at electrode potential (V)				
	100 V	250 V	500 V	1000 V	1500 V
1.0	38.0	97.5	100.0	100.0	100.0
2.0	19.2	48.3	97.5	100.0	100.0
4.0	9.5	25.0	48.3	97.5	100.0
6.0	6.5	16.5	32.8	65.4	97.5
8.0	4.8	11.7	25.0	48.3	73.4

TABLE IV. Fraction of secondary electrons within an energy window.

Nominal energy E_s (eV)	Energy window ΔE_s (eV)	η_{exe} (%)
4.0	$\pm$ 0.25	4.4
4.0	$\pm$ 0.50	8.5
4.0	$\pm$ 1.00	15.9
4.0	$\pm$ 2.00	27.9
4.0	$\pm$ 3.00	36.5
4.0	$\pm$ 4.00	41.1

The optical properties of low-energy electron lenses can be computed from the numerical solution of the electrostatic potential problem and the subsequent integration of the charged particle trajectories through the fields. An invaluable compendium of electron optical properties of common electron lens configurations has been compiled by Harting and Read.[67] The electron optical design problem is to transport the electrons from the sample region extraction electrode, now at a potential of 500–1500 V, to the detector plane at a potential of 150 V. In our system , the quarter sphere necessarily breaks the symmetry of the transport optical column. If a beam of electrons is incident on the quarter sphere in a parallel bundle, then at the exit to the quarter sphere, the distribution of trajectories is focused to a point. Since we require that the electron beam envelope entering each of the detectors be equivalent, extra lenses must be included in either the "straight-through" or "right-angle" leg of the transport optics. If this is done, the beam profile at both detectors can be equivalent except for the effects of dispersion in the quarter sphere.[68]

In Fig. 8, a cross section of our transport optics system is shown. Secondary electrons are extracted from the sample by an extraction electrode E_1 at 1496 volts and enter the column through aperture A_0. Since the nominal design kinetic energy of the secondary electrons is 4 eV, the kinetic energy of the electrons as they enter the electron optics is 1500 eV. The virtual object position for the first lens of the transport optics is shown. Electrons are focused to a minimum beam diameter, or waist, at aperture A_1 by the einzel lens composed of electrodes $E_1 - E_2 - E_3$. Deflector D_1 is used to align the beam with the center of A_1. The einzel lens composed of electrodes $E_3 - E_4 - E_5$ is used to form the next beam waist at aperture A_2. Deflector D_2 is used to align the beam with the center of this aperture. Deflector D_2 has a secondary function which will be described later. Aperture A_2 is essentially the beam defining aperture, which limits both the spatial and angular extent of the beam. It further limits the energy spread in the beam through the large chromatic aberration present in the long focal length einzel lens composed of electrodes $E_3 - E_4 - E_5$. The lens composed of electrodes $E_5 - E_6 - E_7$ focuses the beam to another minimum waist at aperture A_3. This is the object point for the quarter-sphere deflector. Electrode E_8 together with the quarter-sphere deflector form a lens that will force the two separate legs of the system to have equivalent beam envelopes. When the quarter-sphere potential is 340 V, the beam is not deflected and the straight-through detector is selected.

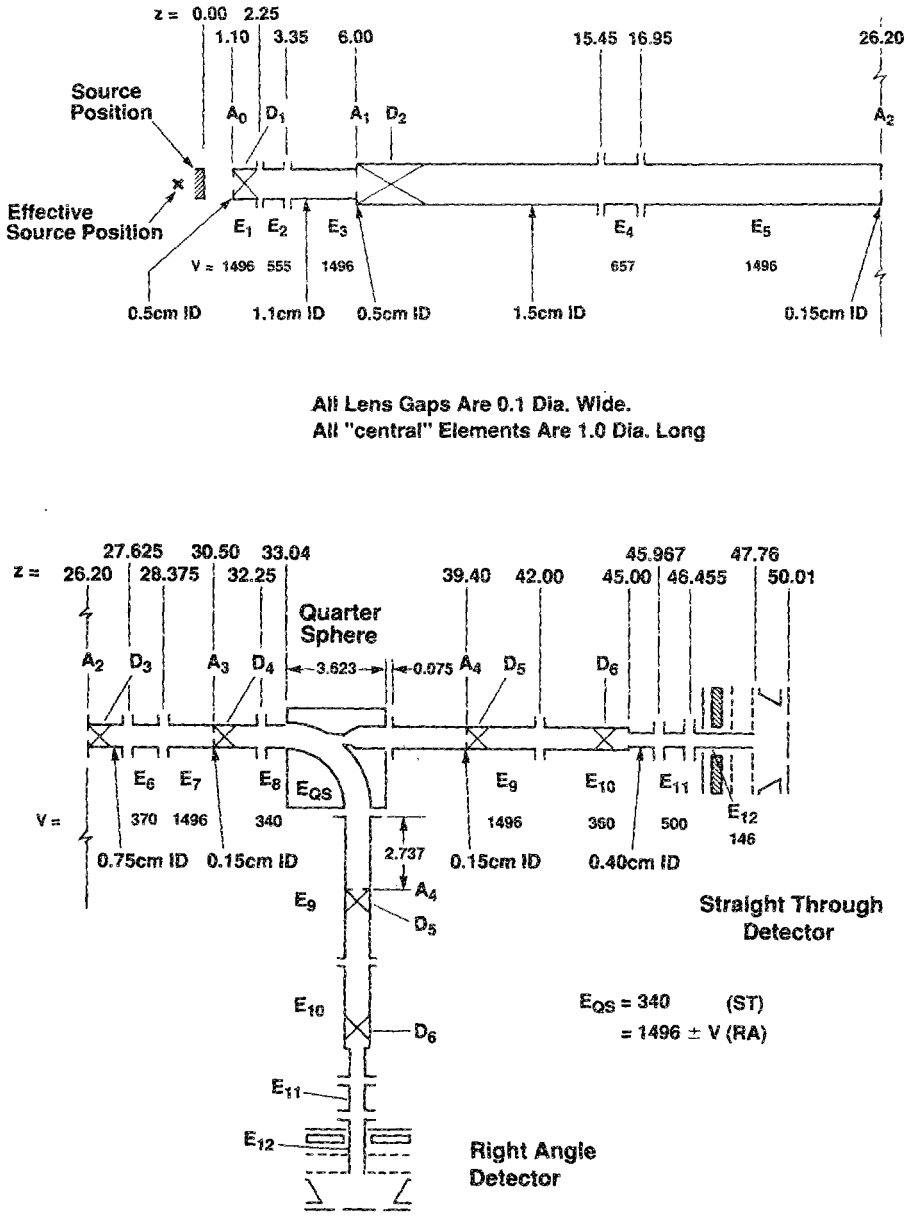

FIG. 8. Transport optics currently used in our SEMPA system. The system uses two detectors: the "straight-through" detector to analyze in-plane polarization component and a "switch-yard" and a "right-angle" detector to measure the out-of-plane polarization and a redundant in-plane component.

When the quarter-sphere pass energy is 1500 V, as indicated on Fig. 8, the beam is deflected by 90° and the right-angle detector is selected. The optional aperture A_4, is present to block any stray electrons generated in the quarter-sphere from entering the detector. The final zoom lens composed of electrodes $E_9 - E_{10} - E_{11}$ is used to focus the electrons onto the Au foil in the detector while reducing the beam energy to the necessary 150 eV. Deflectors D_5 and D_6 can control the angle and position, respectively, of the beam at the Au foil plane. We have found that the extracted electrons that are allowed to enter the SEMPA transport optical column can be transmitted to the detector with nearly 100% efficiency for a properly aligned beam.

The deflector D_2 in the transport optics performs a dual purpose. Besides the static deflection for beam alignment, it is also a dynamic element. This deflector is an octupole with a dynamic descan incorporated from the electron probe-forming column control electronics. We mentioned that instrumental asymmetries can severely degrade the performance of the SEMPA detectors. We alluded to the possibility of a compensation scheme, which we will discuss. However, it is also possible to dynamically remove the asymmetry due to the beam scan by forcing it to be stationary on the detector's scattering foil. When the beam in the electron microscope column is rastered by the deflection coils in the column, the spot is moved across the sample surface. This means that the object position for the SEMPA optics is moving as well, making the object seem as large as the scan field. One way of compensating for this is to use the signal that has been generated to drive the scan coils in the electron optical column to "descan" the beam within the SEMPA transport optics. We take the scan signal from the column and feed it into the octupole descan deflector D_2 180° out of phase with the original scan. Thus, the beam is deflected back onto axis at aperture A_2. We can effectively remove all of the scan-generated instrumental asymmetry in our system for scan fields as large as 70 μm at the specimen using this technique. Although aberrations in the deflection become apparent for

scan fields larger than 150 μm, we are able to see magnetic images in real time for scan fields as large as 500 μm in otherwise uncompensated detectors.

The other technique for eliminating or reducing the instrumental asymmetries due to scanning in SEMPA is to use compensation at the spin analyzer as described in Sec. IV B. It is desirable to implement both a descan correction and a compensation of the detector in order to remove most fully all instrumental artifacts.

Recall that the compensation condition requirements given in Sec. IV B indicated that a linear relationship existed between the tilt and displacement asymmetries at the Au foil in the detector. In phase space ($[\mathbf{r} - \Theta]$ space that for this problem can be separated into two subspaces $[x - \Theta_x]$ and $[y - \Theta_y]$ relevant to measuring the two orthogonal components of the electron spin in the detector), the compensation condition is a straight line. In other words, if a trajectory strikes the foil at some displacement from the central axis, then it must also strike the foil at the "magic" compensation angle where the displacement and angular instrumental asymmetries are equal and opposite. Thus, the second desired function of the transport optics is to map the incident region of phase space for any experiment onto the Au foil such that the final phase space map matches the compensation condition.[52] We have optimized the input optics of the LEDS detector for variations in the position of the beam, characteristic of beam wobble for polarized photoemission studies. We found that, using the compensation technique, we were able to reduce the displacement asymmetry from 6%/mm to 0.35%/mm over a 4-mm scan field.[52] We are currently in the process of implementing this asymmetry compensation scheme in addition to the dynamic descan on our SEMPA apparatus.

VI. SIGNAL PROCESSING ELECTRONICS

Each detector determines two components of the spin polarization vector through the measurement of the collected electron current in opposing detector quadrants and the use of Eqs. (5) and (6). It is the function of the data acquisition electronics to make stable, low noise measurements of the collected electron current. The circuitry required depends, in large measure, on the current expected to reach the electron detectors. For low currents, as might be expected when the electron probe beam is focused to very high resolution, individual pulse counting is necessary to avoid the noise introduced by analog devices and to maintain the high data acquisition rates desired for images. At high currents, which are available in a microscope with a LaB_6 cathode operated at moderate resolution, analog signal processing becomes necessary. This is because of the count rate limitations of microchannel plates (MCP) operated in the saturated or pulse counting mode.

Microchannel plates are generally considered to have a linear response up to an output current of 10% of their strip current.[69] When used for pulse counting, their operating characteristics can be more complex. For example, because of the statistical nature of the charge multiplication process, not all input electrons cause the same size pulse of output charge. However, a well-defined pulse height distribution is necessary to allow a discriminator to trigger on each signal pulse but effectively eliminate most background noise. Such a pulse height spectrum is best obtained from channel plates with channel aspect ratios, length to width of 80:1.[70] Further, to avoid problems with ion feedback,[71] channel plates are often operated in the chevron configuration where the channels of the first plate meet those of the second plate at a slight angle. If a gap is left between the plates in the Chevron configuration, the pulse height spectrum will then depend upon the field between the plates, as the field controls how many channels of the second plate are excited by a single event in the first plate.[71] Currently, satisfactory pulse counting operation is obtained with no gap between plates. Moire effects have not been observed.[72] For example, in a three-plate configuration, an average of seven channels are excited in the final plate.[72,73]

In order for the charge pulse to be discernable from noise, sufficient gain must be available, but this gain will decrease at high count rates. This is because the charge that comes from a single channel of the second channel plate comes from near the end of the channel and must be replenished by the power supply. Otherwise, the field at the end of the plate will be lower, the secondary coefficient will decrease, and the charge multiplication process will be greatly reduced. The time it takes to recharge the channel depends on the channel plate conductance and capacitance[69,74] and will be several milliseconds for typical channel plates. This effect, referred to as charge saturation, limits the maximum count rate. However, if the incident electron flux is roughly uniformly distributed over the channel plate surface, then the probability of a second pulse in the "dead" channel is reduced in proportion to the total number of channels. With increasing count rate, some channels will be triggered before they are fully recharged and the modal gain, i.e., the gain corresponding to the peak of the output pulse height distribution, will begin to decrease.[75] In continuous operation, the output current can, at best, approach the sum of the input current and the bias current. This causes a nonlinear relationship between input and output when the output current exceeds about 10% of the wall current. The relationship between the system's overall particle detection efficiency and count rate will depend in detail on the level of electronic amplification, the discriminator setting, and the shape of the pulse height distribution function. Occasionally, the literature[69,74] describes linear, "pulsed" operation seemingly above the 10% current limit given above. This refers to gating the incident flux off for several milliseconds to allow the channels time to recharge between brief exposures to a high incident flux. The instantaneous output currents can then exceed the 10% limit or even the bias current.

The requirement of a linear transfer function imposes a count rate limit of, $r_{max} = 0.1 I_{bias}/(eG)$, where I_{bias} is the channel-plate bias, e is the electron charge, and G is the gain. For a two-plate chevron assembly operating with an overall gain of 10^6, a typical second-stage channel plate, 40 mm in diameter[76] with 25-μm-diam channels, would have a bias current of 4 μA and a maximum count rate of 625 kHz/quadrant. Similar channel plates are now available with bias currents of 160 μA and a maximum count rate of 25 MHz/quadrant.[77]

If the count rate limitations of the channel plate are acceptable, then care needs to be taken in the rest of the counting chain to ensure reliable operation. For example, the quadrant anode structure must be designed to minimize cross talk between adjacent channels.[78] Otherwise, pulses from adjacent channels will appear at reduced amplitude and fill in the valley in the pulse height spectrum below the peak, making pulse discrimination more uncertain. This effect is easily diagnosed by comparing the pulse height spectrum of an individual quadrant to that of all quadrants connected together. Reduction of interanode capacitance and capacitive coupling from each anode to common surrounding surfaces, including the rear channel-plate surface, is effective in reducing this problem. Fifty-ohm cabling, feedthroughs, amplifiers, and discriminators should be used if voltage-sensitive detection is used. Preamplifiers with bandwidths of 1 GHz and 300 MHz discriminators are readily available.[78] It is most convenient to have a blocking capacitor internal to the vacuum system so that low-voltage feedthroughs can be used. Alternatively, a charge-sensitive preamplifier could be used, but its speed may further reduce the maximum count rate below the maximum set by the microchannel-plate linearity requirement.

Pulse widths of less than 1 ns are common in stacked microchannel plates[11] and facilitate high-speed counting. Dark currents of less than 1 count/cm^2/s are typical. Local noise sources or hotspots are usually associated with dust particles on the surface[79] which can be minimized with careful handling.

For high detector current levels, the channel-plate bias voltage is decreased to establish a linear transfer function and analog detection is used. Each pair of channels consists of two matched current-to-voltage converters, followed by function modules that calculate the sum and difference of the two quadrant signals. The sum and, after amplification, the difference signals are converted to a pulse train by separate voltage-to-frequency converters. Pulse transformers provide the isolation necessary for the input stages to operate at the microchannel plate anode voltage and the signals are counted with a conventional scaler and timer system. Since the difference signal may change sign, an offset voltage of 60% of full scale is applied to that voltage-to-frequency converter to prevent zero crossing and minimize digitization errors. For analog detection, the signal path out of the vacuum system should use guarded feedthroughs floating at the anode voltage to minimize noise due to leakage currents.

The computer controlled data acquisition system includes four 16-bit scalers and a timer. Data are accumulated as 16-bit integers, but are scaled by the relevant maxima and minima and stored on disk as 8-bit integers. The data system controls the digitally derived microscope scan voltages, the dwell time at each point, and the dimensions of the scan data array.

The convenience with which these parameters can be changed and the shortest time it takes to acquire a magnetic image both have a significant impact on the ease of use of a SEMPA instrument. In a normal SEM, the intensity signal derived from the full secondary emission provides sufficient signal to allow images to be presented at near video rates, greatly facilitating focusing and searching for important structural features. Since the magnetization images are independent of the intensity images, the operator of a SEMPA instrument will sometimes be faced with the problem of locating relevant magnetic structure in a region of indistinct physical structure. For this purpose it is important that the frame rate be as rapid as possible. At the reduced data array size, 64×48, a new image is presented every 2 s. Computer improvements could increase the frame rate to 3 frames/s.

Each data frame can be made to replace the previous one or frames can be accumulated to signal average. Short dwell times can be used and frame averaging can be continued until either a sufficient signal-to-noise ratio is obtained or stage drift becomes a concern at higher magnifications. Single key strokes are used to double (or half) the data array dimensions and toggle between averaging and frame replacement, allowing a simple transformation between surveying the sample and beginning serious data acquisition. A continuous, automatically scaled, live display of the intensity image and two magnetization images is always available.

VII. SYSTEM UNIFICATION AND PERFORMANCE

We have discussed the individual components that constitute the SEMPA system. These elements must be unified into a coherent unit for optimum system performance. The requirements to be met are mainly mechanical. In our instrument, the SEMPA transport and extraction optics must be on a bellows such that the SEMPA apparatus may be extracted during ion sputtering or the acquisition of Auger electron spectra. The SEMPA transport optics and associated detectors should not introduce any extra acoustic noise or vibrations into the probe forming electron optical column. The vacuum requirements of the transport optics, detectors, and the electron optical column should all be compatible. The entire system should be bakeable. The stray magnetic fields in the main chamber and in the entire SEMPA transport optics system should be kept to a minimum. Careful magnetic shielding of the entire system is essential any time that low-energy electrons are involved in an experiment.

The SEMPA system performance can be determined by considering each of the elements in the measurement process serially. Consider the production process of secondary electrons at the specimen surface. Assume that the current incident on the specimen is I_0 and that the probe diameter on the sample is δ. The incident electron beam creates secondaries. The yield is a function of the incident beam energy, the angle of incidence, and the material.[17] The range of secondary electron yields is summarized in Table V. As can be seen, the secondary electron yield is approximately $\delta_{se} = 0.25$–0.40 in the 10–20 keV incident energy range. The secondary yield is enhanced by the $1/\cos \Theta_n$ dependence on the angle of incidence,[17] where Θ_n is the angle of the surface normal relative to the incident electron beam, such that our value of $\delta_{se} = 0.35$–0.55. Assume that $\delta_{se} = 0.45$.

We have already considered the energy and angle collection efficiencies of the transport optics as a function of extraction electrode potential in Sec. V. We concluded that we could achieve adequate performance from an extraction potential of about 1000 V. We found an energy collection effi-

ciency $\eta_{exe} = 0.41$ for a 4.0 eV $\pm$ 4.0 eV energy window. The angular collection efficiency η_{exa} corresponding to this is a weighted sum of the vertical column in Table III for the 1000-V electrode potential. Since there are mostly 4.0-eV electrons, and the distribution of secondary electrons in energy falls off rapidly with energy,[17] the angular collection efficiency of the extraction optics is no less than $\eta_{exa} = 0.90$. The transport optics may have a transmission as high as 1.00, but as a lower bound for normal operation, we have determined that the transport optics between the extraction electrode and the detector has a transport efficiency of $\eta_{to} = 0.875$.

The conversion efficiency for the Au target in the LEDS electron-spin polarization detector has been measured,[50,52] and is the parameter I/I_d discussed in Sec. IV. This conversion efficiency for current incident on the Au target to the current incident on the detector channel plate input is $\eta_{Au} = 0.04$ for nominal operating conditions. The collection efficiency for the entire system is the product of all of the individual collection or transmission coefficients:

$$\eta = \eta_{exe}\eta_{exa}\eta_{to}\eta_{Au}. \tag{14}$$

The total transmission in our system is $\eta = 1.3\%$.

In order to estimate the signal level and integration time required to provide a useful magnetic image, we consider a specific change in polarization and calculate the integration time necessary to reach the signal-to-noise ratio considered adequate for the observation of that change. Let us consider the case of differentiating between two adjacent domains with oppositely directed magnetization. Further, assume that the sample is oriented so that the full polarization is measured by one detector, that is the measured component of P will be $+P$ for one domain and $-P$ for the other. The total change in that polarization component between the two domains, i.e., the signal, is $2P$. The signal-to-noise ratio, SNR, for a polarization image can be estimated most easily for the case of counting statistics, but we will simultaneously consider modifications necessary for analog detection. If the electron microscope beam incident on the sample is represented by a current I_0, then the mean number of particles striking the sample in time τ is $I_0\tau/e$, where e is the electronic charge. Assuming that the number of particles is Poisson distributed with this mean value, then the variance will also be $I_0\tau/e$. Of course, there may be additional noise in the beam, due, for example, to variations in the cathode emission process.

At the sample, each incident electron produces an average of δ_{se} secondary electrons. Because the secondary emission process allows for 0, 1, 2, or more electrons for each incident particle, the noise analysis must include the variance associated with both the incident flux and the variance about the "gain factor" δ_{se}.[80–82] At this point the mean number of secondary electrons is $\delta_{se}I_0\tau/e$ and their distribution is not strictly Poisson distributed. The statistical distribution is mixed and may alternately be described by a Polya distribution,[82] which can range in shape from an exponential to a Poisson distribution. More simply, by restricting attention to the mean and variance of the distribution, one can allow a factor in the variance to represent the additional noise beyond Poisson variation.[80,81]

TABLE V. Characteristic secondary electron yields vs incident beam energy.

Element	$E_0 = 1$ keV	5 keV	20 keV	50 keV
Al	1.0	0.40	0.10	0.05
Au	1.0	0.70	0.20	0.10

From this point until the electrons hit the front of the channel plate in the spin detector, they pass through a number of filters, each characterized by an efficiency η, consisting of η_{exe}, η_{exa}, η_{to}, and η_{Au}. Each of these filters can be modeled as either allowing or not allowing the electron to pass. The outcome only has two values, 0 or 1, characteristic of a binomial trial. Further, the cascade of binomial distributions is itself a binomial distribution while the cascade of a Poisson and a binomial distribution remains Poisson distributed.[82] If we multiply the mean number of secondaries by $\eta_{exe}\eta_{exa}\eta_{to}\eta_{Au}$ we obtain the mean number of electrons at the channel-plate input. Had the mean number of secondaries produced at the sample been Poisson distributed, then this would also equal the variance in the mean value of electrons scattered from the Au, since this quantity would also be Poisson distributed. Since the statistics of secondary production generates non-Poisson distributions, this simple approach does not yield the correct variance. Fortunately, there is a self normalization in polarization measurements due to the fact that in Eq. (5), for example, all of the measured quantities are proportional to the value of the flux incident on the Au target of the polarization detector. Hence, all of the noise sources described so far will be common to both channels A and C, and will not contribute to an error in the polarization measurement.

The backscattering of the electrons at the Au target can be viewed in a similar way. A cross section determines what fraction of electrons of a given spin will arrive in quadrant A at the front of the channel-plate multiplier, and a second cross section is applicable for quadrant C. Whether an electron is scattered or not is a random process and we can therefore characterize this as having a binomial distribution. As the number of particles increases, the binomial distribution approaches a Poisson distribution as a limit. The result is that the number of counts arriving at the channel-plate input are Poisson distributed with variance equal to their mean values. Before reaching the anode of the detector, each electron must hit a sensitive part of the front channel plate surface, a binomial filter with $\eta_{cp} = 0.85$,[73] and have its charge multiplied by the cascade process of secondary emission within the channel-plate assembly. For analog signal detection, we must include the noise present in the gain introduced at this stage.[82] For electron multipliers, where a cascade of secondary emission processes is used to provide gain, the noise is strongly dependent on the first secondary emission coefficient. The noise to be expected can be approximated by defining the anode noise figure to be a factor γ equal to the actual standard deviation in the output divided by that expected assuming Poisson statistics. For the chevron chan-

nel plates used here, a typical anode noise figure of $\gamma = 1.25$ can be expected.[83] However, if the channel plates are operated in the pulse counting mode and exhibit a saturated pulse height spectrum that shows that each incident electron has undergone sufficient multiplication to place it distinctly above a fixed discriminator level, then Poisson statistics can again be expected to apply, and $\gamma = 1$.

Kessler[29] shows that for a particle counting measurement of a polarization $P = (1/S)(N_C - N_A)/(N_C + N_A)$, as defined in Eq. (5), the one standard deviation statistical error is approximately $\Delta P = [1/(N_C + N_A)S^2]^{1/2}$. For analog detection in channel-plate chevrons, this error estimate will be increased by a factor of about 1.25, the anode noise figure γ. Note that in Kessler's approach, the approximate error in the polarization measurement is independent of the value of the polarization. This is not strictly true for large values of the polarization.[84]

After substituting $I_0\delta_{se}\eta\eta_{cp}\tau/2e$ for $(N_C + N_A)$, we can calculate the signal-to-noise ratio for pulse detection,

$$\mathrm{SNR} \equiv 2P/\Delta P = 2PS(I_0\delta_{se}\eta\eta_{cp}\tau/2e)^{1/2}. \quad (15)$$

Solving for τ gives us the dwell time required for each pixel in the image as a function of the desired signal-to-noise ratio and the experimental parameters:

$$\tau = (\mathrm{SNR})^2 e/(2P^2S^2I_0\delta_{se}\eta\eta_{cp}). \quad (16)$$

Now assume that the channel plates can be used in pulse counting mode and that the maximum counting rate is 10 MHz per quadrant. This will impose an upper limit on the useable current in the column to be in the range of 1 nA. Assume that $I_0 = 1$ nA. The dwell time per pixel in our implementation will be $\tau = 1.33(\mathrm{SNR})^2/P^2\ \mu$s. In Table VI a summary of pixel dwell times is given for various desired signal-to-noise ratios, and various polarizations, under the assumptions given above with an incident beam current of 1 nA. In electron microscopy, a signal-to-noise ratio of 5 is considered adequate to distinguish a signal change.[17] However, frequently domain images with lower signal to noise figures are acceptable because of the tendency towards visual averaging within the distinct domains.

To translate the figures in Table VI into magnetic image acquisition times, the elements in the table must be multiplied by the number of pixels in an image. Thus, it takes about 54 s to acquire a 256×256 pixel image with a signal-to-noise ratio of 5 and a mean polarization of 0.20 (with all of the assumptions made above such as $I_0 = 1$ nA and $S = -0.11$.

TABLE VI. Pixel dwell times as a function of the desired SNR and beam polarization.

	Pixel dwell time τ(ms), I_0 = 1 nA			
P	SNR = 2	SNR = 3	SNR = 5	SNR = 10
0.01	53.185	119.666	332.407	1329.626
0.10	0.532	1.197	3.324	13.296
0.20	0.133	0.299	0.831	3.324
0.40	0.033	0.075	0.208	0.831

We now consider an example of a measurement of a domain wall profile where the resolution of a large number of polarization levels is desired and a large acquisition time may be necessary. While the acquistion time may be unlimited in principle, realistic time limitations are imposed by stage drift, beam heating of the sample, sample contamination, and miscellaneous long time constant instabilities within the electron optical column. We consider an instrument with a probe size of 10 nm and a probe current of 1.0 nA. An instrument with these specifications at a 10-mm working distance is characterized as a high performance SEM. Suppose that drift and other instabilities limit the total acquisition time to 25 min. We will make a measurement composed of a single 128 pixel line scan across the domain wall. The dwell time per pixel must be less than $\tau < 11.7$ s. The polarization is $-P$ on one side of the wall and $+P$ on the other side. If we wish to discriminate N levels within the magnetization profile of the wall, then the signal of $2P$ that was used in Eq. (15) must be replaced by $2P/N$. Let us choose $N = 20$. Given the time constraint, we can determine a minimum detectable polarization P_{min} for a line scan of a given signal-to-noise ratio for a wall profile resolved into N levels. The minimum detectable polarizations above are given in Table VII for various signal-to-noise ratios.

We know of three operational SEMPA systems, and several others that are being built. In Fig. 9(a), a schematic of the Koike *et al.*[13,49,85–100] SEMPA system is given. Their system utilizes a cold field emission source in a standard SEM optical column. They analyze the polarized electrons with a conventional high-energy (100 keV) Mott detector. Their spatial resolution for SEMPA is near 30 nm.[13] They have used their system to study the micromagnetic structure of Fe,[13,86,89,92,100] SiFe,[13,87,89,100] an Fe polycrystal,[13,88–90,93,100] Co,[13,89,91,100] permalloy thin-film heads,[13,94,96–98] surface Néel walls,[13,96,98] and written bits.[13] In Fig. 9(b), the SEMPA configuration of Kirschner *et al.*[14,44,101,102] is shown. They have a field emission electron source in a standard SEM electron optical column and a LEED detector. Their SEMPA spatial resolution is near 40 nm.[102] They have used their system to study a surface Néel wall in Fe.[14,101,102] We have shown a schematic of our SEMPA apparatus in Fig. 2, the details of our LEDS detector in Fig. 4 and the complete transport optics in Fig. 8.[15,103–117] This system has been used to study FeSi,[15,104–109,111–115] ferromagnetic glasses,[15,112,114] thin-film permalloy heads,[15,112] surface Néel walls,[15,115–117] thin permalloy films,[115–117] and uniaxial Co.[114,118] We routinely achieve a spatial resolution of 50 nm when acquiring magnetic images in our present system.

TABLE VII. P_{min} for a wall profile divided into 20 polarization subintervals for a 10-nm resolution SEMPA measurement. $I_0 = 1$ nA and a 128 pixel line scan is assumed.

	SNR = 1	SNR = 2	SNR = 3	SNR = 5	SNR = 10
P_{min}	0.0067	0.013	0.020	0.033	0.067

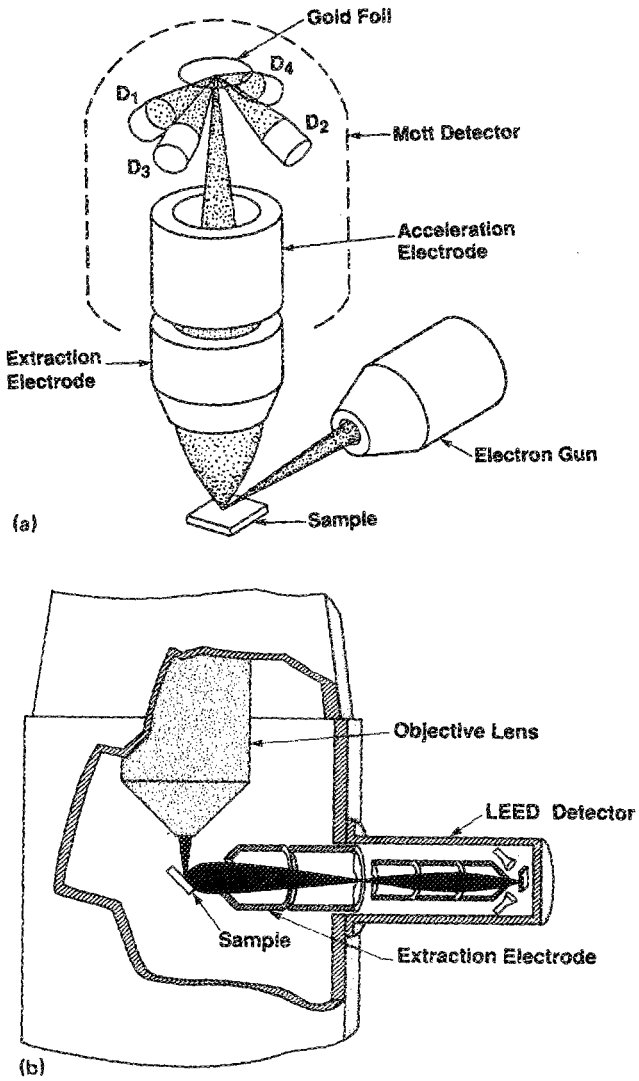

FIG. 9. (a) SEMPA system developed by Koike and co-workers (Ref. 13). (b) SEMPA system developed by Kirschner and Oepen (Ref. 14).

VIII. DATA PROCESSING AND EXAMPLES OF SEMPA IMAGES

Each time data are acquired in a SEMPA experiment, either the polarization and the intensity signal, or the left and right detector signals, may be stored. Both of these alternatives are functionally equivalent, although we have found it more convenient to do the subtractions and additions in hardware, as prescribed by Eqs. (5) and (6). Additionally, if the detectors are configured in pairs[13,15] such that two components of the spin polarization can be recorded simultaneously, two independent sets of data are acquired simultaneously. In the ensuing discussion, we will describe the analysis for the images in the "straight-through" detector in our SEMPA system in Fig. 2. The two components of the polarization that are measured are the in-plane (in the plane of the sample surface) components P_x and P_y.

The spin polarization for a representative sampling of the valence band by exciting electron-hole pairs can be estimated from the number of total valence electrons/atom in the metal n_v and the number of Bohr magnetons/atom n_B. The number of Bohr magnetons/atom is found by determining the difference in the number of "spin-up" and "spin-down" electrons per atom. We estimate that the average magnitude of the polarization measured in SEMPA will be $P = n_B/n_v$, and summarize the results in Table VIII. Further, spin-dependent mean free path considerations[27,28] enhance the value of the polarization in the low secondary electron energy region. The magnetization direction is in the opposite direction to the electron-spin direction. For 3d transition metals, the magnitude and the direction of the magnetization can be determined from measuring the polarization, and hence we present magnetization maps. For more complicated systems, such as the rare-earth transition-metal systems, the rare earth elements introduce $4f$ (polarized) electrons. These electrons are not easily excited in the secondary electron cascade. Thus, the SEMPA signal from a system such as TbFeCo will be proportional primarily to the FeCo subnetwork.[119]

The images are stored in P_x, P_y, I_x, and I_y data structures. The individual signals from the four separate quadrants of the detector (inset of Fig. 4) can be recovered simply. Although the data are recorded in 16-bit format, they are stored in 8-bit format after rescaling. The hierarchy of data processing steps for vector magnetic images is given below.

A. Data processing

Instrumental asymmetries are caused by inhomogeneities in the spin detectors, unequal gains in the channels of the signal processing electronics and beam misalignment within the detector. Each of these effects will produce an error in the measured spin asymmetry. When the beam is scanned as it is in SEMPA, the beam within the detector moves, causing scan-related instrumental asymmetries. We discussed the compensation and descan methods for removing most of the scan-related asymmetry. Even so, for large scan fields ($> 150\ \mu$m), residual scan asymmetries exist in the magnetic images. These scan asymmetries are removed in the processing of the data. Any zero offset in the polarization measurement may also be removed in data processing. Finally, a third type of instrumental asymmetry may also be present in highly corrugated samples. This asymmetry is the result of topographical effects on the sample surface that may cause electrons to be emitted from the surface at "unusual" angles. These skewed trajectories are imaged onto the detector target where they can produce spurious asymmetries. These asymmetries result directly from electron trajectory effects at the sample surface. These asymmetries are

TABLE VIII. Estimated polarization for 3d transition metals.

Metal	n_B	n_v	P
Fe	2.22	8	0.28
Co	1.72	9	0.19
Ni	0.54	10	0.054

characteristic only of the particular sample surface and extraction field. There is no systematic way to remove these effects for all samples electron optically. Therefore, we introduce an additional scattering target in the detector to accomplish this.

Two separate scattering targets are included in the LEDS spin detector. The Au target, which is used for spin analysis can be rotated on a rotatable feedthrough such that it faces an Au evaporator. The evaporator is used to renew the surface of Au on the target every few days. When the Au is rotated towards the evaporator, another target faces the beam. We use a graphite scattering surface for this target. Graphite, with $Z = 6$, has an extremely low Sherman function, such that both spin-up and spin-down electrons are essentially scattered isotropically. This target can be used to remove any spurious effects which result from trajectory related instrumental asymmetries. These spurious effects are the results of (1) scan-generated instrumental asymmetries which are not completely removed by the descan unit, and (2) aberrant electron trajectory related asymmetries resulting from large surface topography effects. Each SEMPA image acquired with the Au detector target can be associated with a corresponding image taken with the graphite target. We stress that this is only necessary for situations where the surface topography of the sample perturbs the trajectories enough to introduce spurious instrumental asymmetries into the measurement. When a graphite image has been recorded in the identical conditions to the original SEMPA image, and the two images are registered, then the graphite image can be subtracted from the Au target image to remove or reduce topographic "feedthrough."

The first operation in the data processing sequence is the multiplication of the images by -1, thus changing the images from polarization maps into magnetization maps. These images may have some remaining instrumental asymmetries which must be removed. One technique is to acquire a graphite image (once again, both components P_x and P_y of the graphite image are acquired simultaneously) and to subtract it from the SEMPA image for each magnetization component. An alternative, for images where there are no obvious topographic feedthrough trajectory asymmetries, is to fit the image with a plane to remove the residual instrumental asymmetries. For all but the lowest magnification images, where the asymmetry becomes nonlinear, we subtract a background plane. This is done automatically by sampling the image at a number (> 20) of points of identical domain orientation and doing a linear least-squares fit. In the case where the domain structure is complicated and domains of similar orientation cannot be identified, then one must rely on the graphite image subtraction method. Once the background subtraction of the images has been performed, then the zero offset must be corrected. The zero offset correction is the result of having an arbitrary zero in the polarization detector.[29,33]

The offset calibration of spin-polarization detectors is extremely difficult when the incident beam polarization cannot be modulated in order to find the zero of the asymmetry. In general, each measurement's precision is high, but the absolute value may be slightly offset. To determine the zero offset in the SEMPA images, line scan profiles across the domains can be analyzed. When the domain structure is oriented symmetrically on the surface, the identification of this offset is easiest. In the case where the domain structure is more complicated, errors in subtracting the zero offset will be revealed in subsequent data processing. Once the offsets have been identified and subtracted from the images, the magnitude and angle of the magnetization maps can be determined.

There are several formats to represent the data. We use two data formats: the first uses the projection of the magnetization on orthogonal axes, i.e., M_x and M_y, and uses a grey map color scheme where white (black) represents the maximum value of the magnetization in the positive (negative) directions. The second format uses the magnitude $|M|$ and the angle Θ of the magnetization vector projected on some plane with various color mapping schemes. Whether or not it is easier to identify a surface magnetic domain structure in M_x and M_y images or in $|M|$ and Θ images depends largely upon the surface magnetic microstructure.

For all but the hardest magnetic materials, we expect that the magnetization vector should lie entirely in-plane. This is even true for Bloch walls, which terminate at the surface in surface Néel walls,[117] as we shall show shortly. The magnitude of the magnetization is determined as

$$|M| = [M_x^2 + M_y^2 + M_z^2]^{1/2} \tag{17}$$

and the direction with respect to the positive x axis of the in-plane magnetization is (in the absence of any out-of-plane components)

$$\Theta = \tan^{-1}(M_y/M_x). \tag{18}$$

The magnitude of the magnetization should be uniform. We use the magnitude of the magnetization as a precise check on the accuracy of our data processing.

This constitutes the basic data processing sequence. Other features such as image rotation, image expansion, multiplication by scalar constants, addition and subtraction of scalar constants, filtering and line scanning, which are standard image processing routines, are also possible. Once the data have been processed, it can be represented by a black and white image (map) comprised of 256 grey levels or it may be represented by a pseudo-color image (map) comprised of 256 color levels. It is most important to represent the angle maps using psuedo-color representation. The color in the maps must be multivalued. The direction (color) corresponding to 0° and 360° must be the same. This can only be implemented using pseudo-colors if no color in the mapping is to be repeated. We will show examples of pseudo-color representations.

B. Examples

In Figs. 10(a)–10(d), images of the surface magnetic domain structure for a FeSi (100) surface are shown. The surface was ion sputtered with a 1-keV argon beam, and the surface was reannealed at 700 °C. The 256×192 pixel images, 253 μm across, were obtained with an incident beam current of 15.5 nA, and a dwell time of 4.0 ms/pixel. These images took about 3 $\frac{1}{2}$ min to acquire. In Fig. 10(a) the stan-

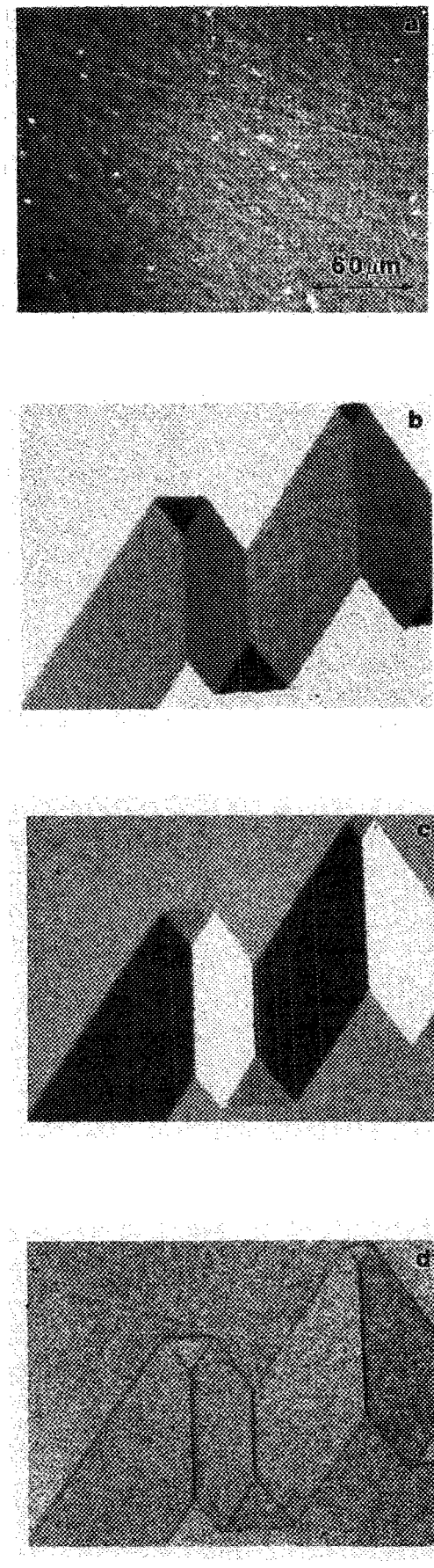

FIG. 10. Images of FeSi (100) surface. Images are 253 μm across. (a) Secondary electron intensity image, (b) M_x, (c) M_y, and (d) $|M|$ images.

dard secondary electron intensity image is shown. The mottled surface is clearly visible, although the surface is relatively flat and smooth. The x component of the magnetization vector M_x and the y component of the magnetization vector M_y are shown in Figs. 10(a) and 10(b), respectively. No graphite images were recorded for this image since there were no asymmetries present of topographical origin and the backgrounds were removed by plane subtraction. In this and all black and white SEMPA images, white corresponds to magnetization along the positive direction while black corresponds to magnetization in the negative direction. In this and all the SEMPA images to be presented, positive **x**, **y**, and **z** point to the right, up, and out of the page (towards you), respectively. FeSi is a magnetic system characterized by cubic magnetic crystalline anisotropy. The easy axes, the direction along which the magnetization vector points in its lowest energy configuration, are along the Cartesian axes. It is energetically unfavorable to have the magnetization pointing out of the surface due to the magnetostatic energy that would result. Therefore, on the surface of any cubic anisotropy material, there are four easy directions in the surface, and should therefore be four principal domain directions. These can easily be identified by the white and black regions in Figs. 10(b) and 10(c).

In Fig. 10(d), the magnitude of the in-plane magnetization vector is given. As can be seen, the image is essentially structureless, except for dark lines at the domain wall boundaries. The dark lines at the domain wall boundaries are artifacts from the measurement, and do not imply that the magnetization is reduced at domain walls. These artifacts are the result of a finite probe size sampling a vector signal, that is, a probe that is larger that the domain wall samples the magnetization on either side of the domain. As the magnetization has the opposite sign on either side of the domain wall, the measured signal for the magnetization is necessarily decreased. This produces minima in the magnitude of the magnetization distribution across domain walls.

To understand the details of the artifact quantitatively, examine the experiment as depicted in Fig. 11(a). This is the model of a 180° domain wall on the surface of Fe. On the left(right) the magnetization points along the negative(positive) y axis. The domain wall is in the center. Detailed studies of domain wall profiles at surfaces have been undertaken,[102,117] and results of these studies will be shown later to illustrate the quantitative results available from SEMPA. For now, assume that the wall profile varies sinusoidally across the interface as $M_x = M_s \cos(x/W)$, and $M_y = M_s \sin(x/W)$, for a wall width of W. Assume that the probe intensity is Gaussian distributed, of width δ. The loss of the magnetization signal across the wall results from the convolution of the finite probe size with the magnetization distribution in the wall. This two dimensional convolution has been done numerically and the results for $W = 150$ nm and 200 nm are given in Fig. 11(b). The minimum magnetization at the center of the wall, is shown as a function of the sampling probe diameter δ for two "idealized" wall widths W. The solid lines are included to guide the eye. Also shown are the measurements of the magnitude of the magnetization in the center of the walls as a function of probe size. The

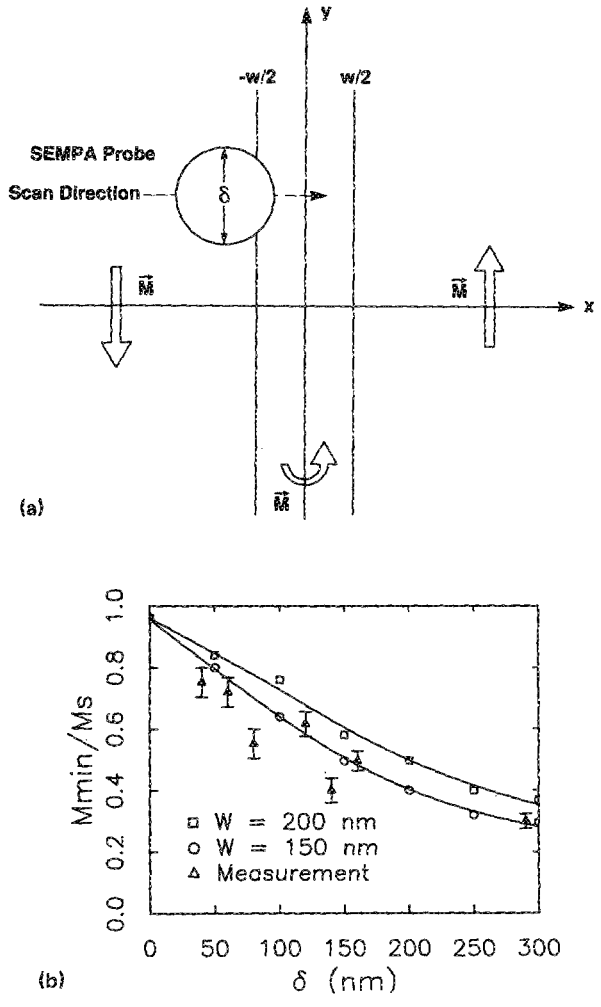

FIG. 11. (a) Schematic of finite-sized probe that samples a 180° domain wall causing some magnetic information to be lost. (b) Lost polarization due to the finite beam size in a surface wall of Fe. Measured and calculated values for the dip in the $|M|$ distribution at the center of the wall as a function of probe diameter δ.

agreement is qualitatively good, the disparity resulting mainly from the simplified model of the wall structure.[117] To avoid any loss of information in the domain walls, the incident probe size must be selected judiciously. We have obtained results where the magnitude of the magnetization is as expected from these arguments, and is constant across a domain wall.[117]

In Fig. 12 we present data from a single-crystal Fe (100) whisker surface that has been ion sputtered with 1-keV argon and reannealed at 700 °C. The image is 85 μm across. The whisker itself is about 32 μm wide and several mm long with its long axis oriented vertically. The 256×192 images were recorded with an incident beam current of 8.7 nA and a dwell time of 2 ms/pixel. In Fig. 12(a), the secondary electron intensity image is shown. The top surface of the crystal is in the center, and the left side of the crystal is in the shadow at the left. The sample stage is seen on the right. Electron microscopes have extremely long depth of focus, and we will see the utility of this in these images. In Figs. 12(b) and 12(c) the raw, unprocessed x-component and y-component magnetization images are shown respectively. The four surface domains present in cubic anisotropy materials are clearly visible. Also evident are numerous surface structures in the magnetization images that seem to result from the strong topographic contrast present in the intensity pictures. Since this example will be used to illustrate the complete processing of SEMPA data, it is instructive to compute the raw signals measured by the x-detector quadrants "A" and "C" of Fig. 4. Figures 10(d) and 10(e) show the images recorded by quadrant "A" and quadrant "C," respectively. It is clear that almost no magnetic contrast is seen. The magnetic image is superimposed on a sizeable background signal. Thus in SEMPA long data acquisition times are necessary in order to accumulate reasonable statistics. Finally, since there are many topographic artifacts present on the surface of the images in 12(b) and 12(c), we anticipate that some improvement can be obtained by the subtraction of the graphite images. The images for the x and y components recorded with the graphite target are shown in Figs. 12(f) and 12(g).

The processed images, where the background has been removed by the subtraction of the graphite target image, are shown in Fig. 13. Figures 13(a) and 13(b) show the x and y components of the magnetization, respectively. We can notice two consequences of the graphite subtraction. First, the surface structures that caused the trajectory-related asymmetry at the detector have been greatly reduced, especially in the x component of Fig. 13(a). Second, the magnetization down the side of the whisker is now clear and well-resolved. The images look flat, as they should. The edges of the top surface of the whisker can be identified by the corners of the diamond domain, the rest of the image being from the side of the whisker. The domains that continue down the left side of the crystal are resolved and of the same intensity as those on the surface. No other domain observation technique affords such enormous depth of field. Finally, in Figs. 13(c) and 13(d) are the magnitude and the direction maps for this image. Once again, the characteristic wall intensity loss is seen resulting from the large probe sampling the surface. Note that the 90° walls show less magnetization loss than the 180° walls. Figure 13(e) contains the color wheel representation for the angles in the map.

To illustrate the possibility of measuring all three components of the spin polarization at one time, Fig. 14 depicts images from the surface of an hcp (0001) Co single crystal.[118] The surface of the Co crystal was ion sputtered with a 1-keV Ar beam and the surface was cyclically annealed at 400 °C. The 256×192 pixel images are 18 μm across and the image was recorded with 3.0 nA of current. The dwell time per pixel is 30 ms, such that the total acquisition time is about 25 min. These images have about 80-nm spatial resolution, although our system is capable of 50-nm resolution.[105] In Fig. 14(a) the standard secondary electron intensity image is shown. In Figs. 14(b)–14(d) the x, y, and z components of the magnetization, respectively, are shown. The domain pattern from this sample is extremely complex.[118] In Fig. 14(e), the in-plane magnetization angle, defined in Eq. (18), is shown together with the color wheel specifying the angular map. The in-plane magnetization seems to have a quasi-six-fold symmetry.[118] Furthermore, the out-of-plane

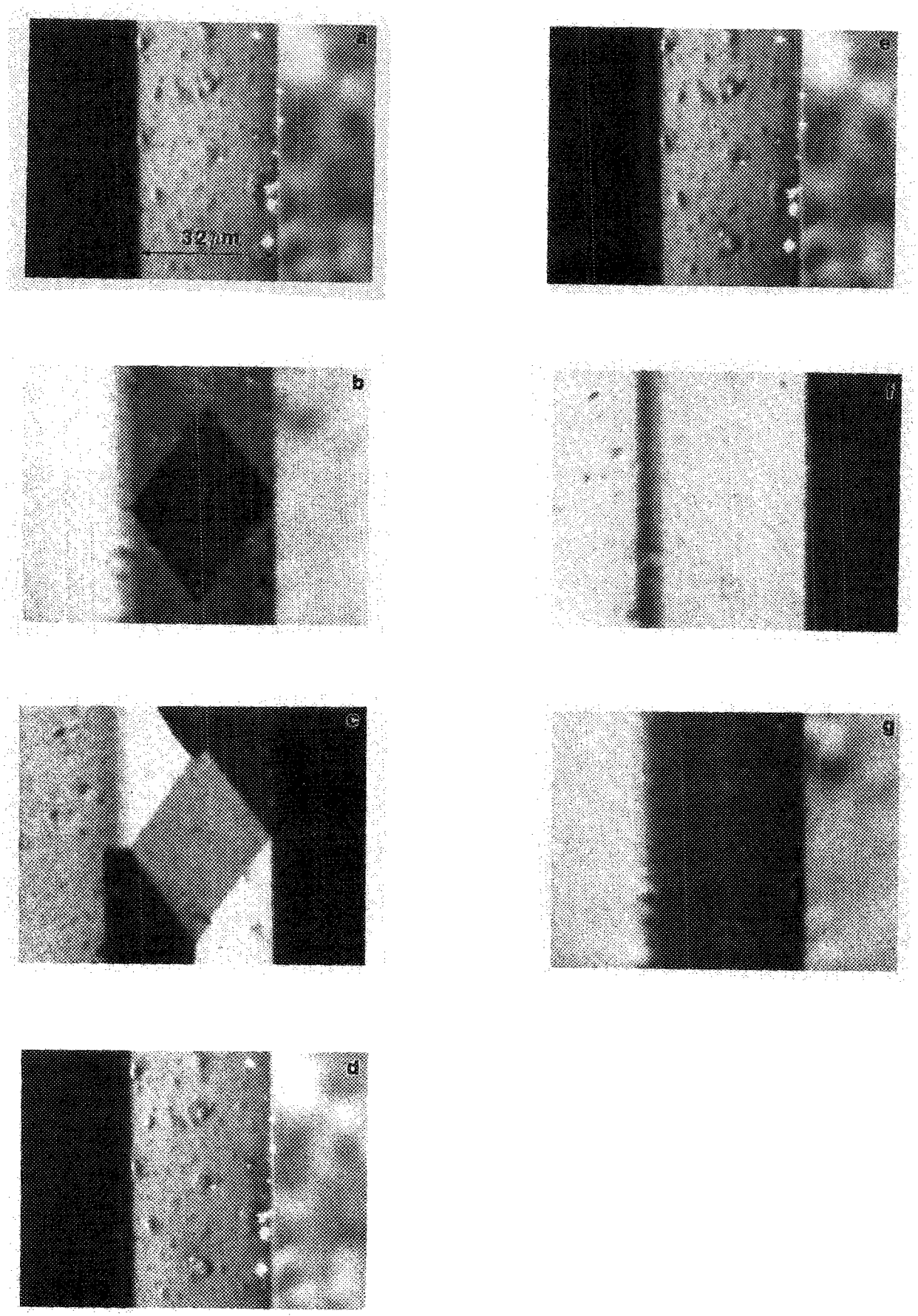

FIG. 12. Images of single crystal Fe (100). Images are 85 μm across. (a) Secondary electron intensity image, (b) raw M_x, (c) raw M_y signals. (d) Reconstructed signal to one quadrant of detector, and (e) the signal on the opposite quadrant illustrating the weakness of the magnetic signal. (f) Graphite image in M_x and (g) M_y used to reduce spurious asymmetries due to trajectory effects from surface topography.

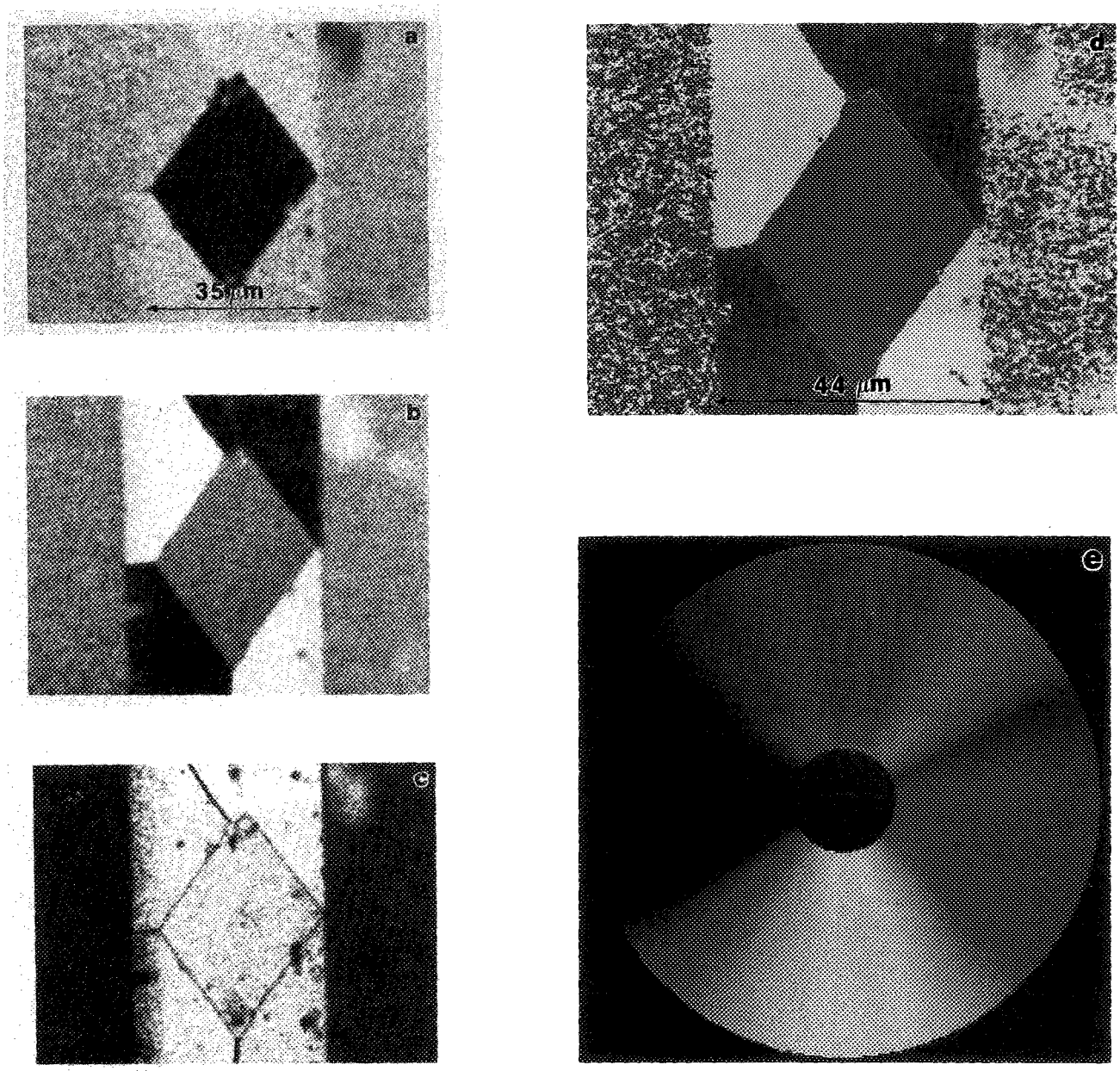

FIG. 13. Processed images of Fig. 12. (a) M_x, (b) M_y, (c) $|M|$, and (d) Θ images with the corresponding color wheel (e) for the angle map.

magnetization seems to serve as a source and sink for the in-plane closure domains at the surface. Similar results from Co have been observed with magneto-optic Kerr effect[120] with necessarily reduced resolution because it is an optical technique.

We conclude our examples with some applications of technological importance. The SEMPA technique can be combined with other surface science analysis techniques to yield micromagnetic and microchemical information. In Figs. 15(a) and 15(b) we show permalloy magnetoresistive, radiation-hard memory elements, which are about 15 μm wide from tip-to-tip of the back of the arrowhead. The structures serve as memory elements by having two stable magnetic states that have different magnetoresistance. Figure 15(a) shows an Auger image using the Ni line at 54 eV while Fig. 15(b) shows the x component of the SEMPA signal. An ion beam was used to sputter the sample with its focus at the right edge of the frame. The memory elements are thinnest near the sputter crater on the right, and get progressively thicker to the left of the sputter crater. The effect that the sputtering has on the magnetization in the film is clear in the image. To the left of the sputter pit, the permalloy elements become thicker and their domains more stable. This example further demonstrates how easy it is to correlate the physical and chemical structure with the micromagnetic structure using this instrument.

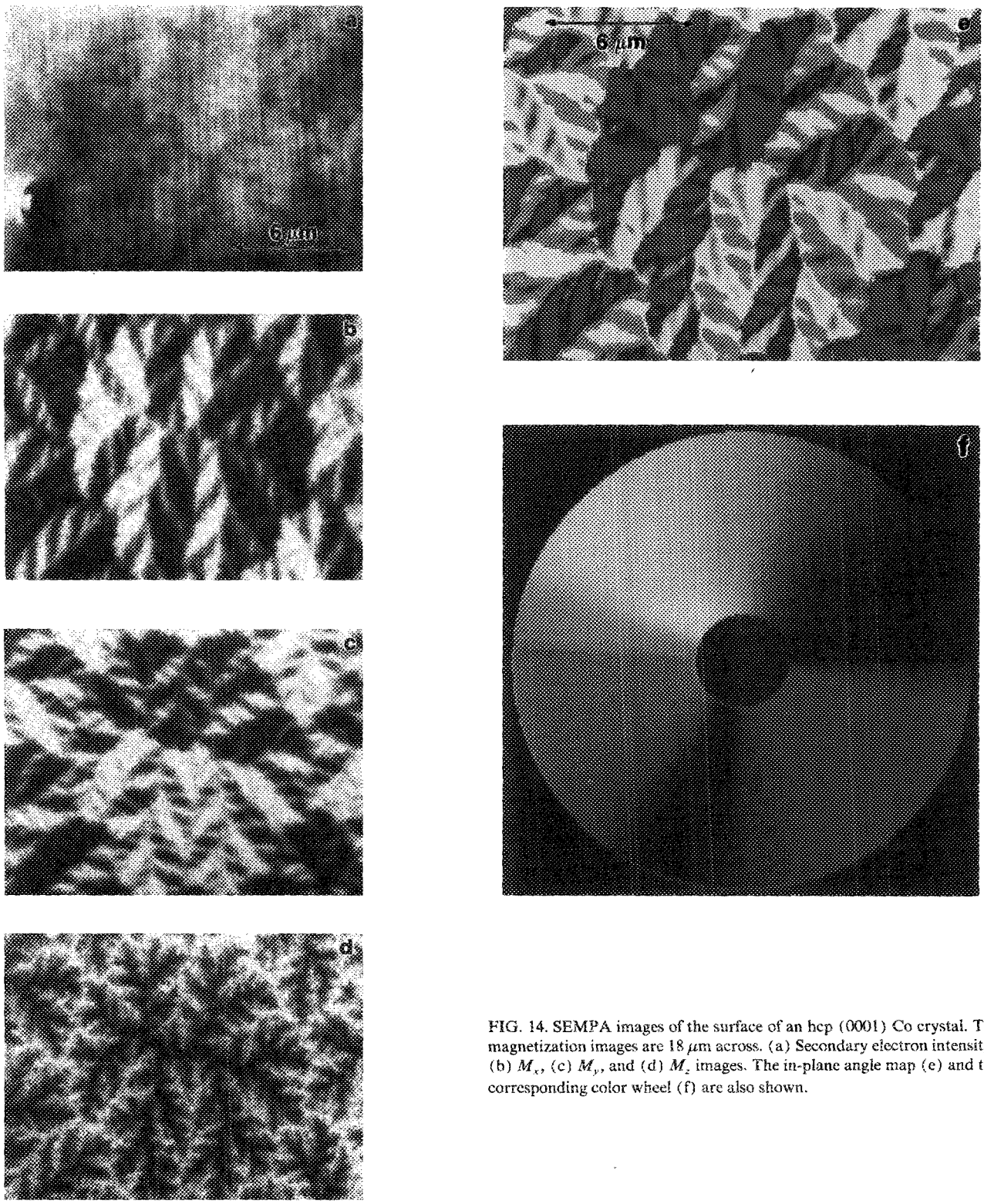

FIG. 14. SEMPA images of the surface of an hcp (0001) Co crystal. The magnetization images are 18 μm across. (a) Secondary electron intensity, (b) M_x, (c) M_y, and (d) M_z images. The in-plane angle map (e) and the corresponding color wheel (f) are also shown.

A second technological example is given by bits written onto 700-Å-thick CoNi hard disk material. The sample was sputter cleaned using 2-keV Ar ions. In Fig. 15(c), a low-density pattern was written onto the disk. This 256×192 pixel image is 25 μm across and shows the well-defined edge profiles for the written bits. In Fig. 15(d), a high-density pattern is used to write bits onto the same medium. This 256×192 pixel image is 12.6 μm across. The dwell time per pixel is 4 ms. The ragged edge transitions are characteristic of noisy media and are clearly visible. The size scales involved here would prohibit the observation of this phenomenon with any optical technique, and thinning the specimen for viewing by TEM Lorentz microscopy would destroy the domain patterns. SEMPA appears to be a unique technique for such observations of magnetic microstructure.

Finally, we show the x and the y components of the

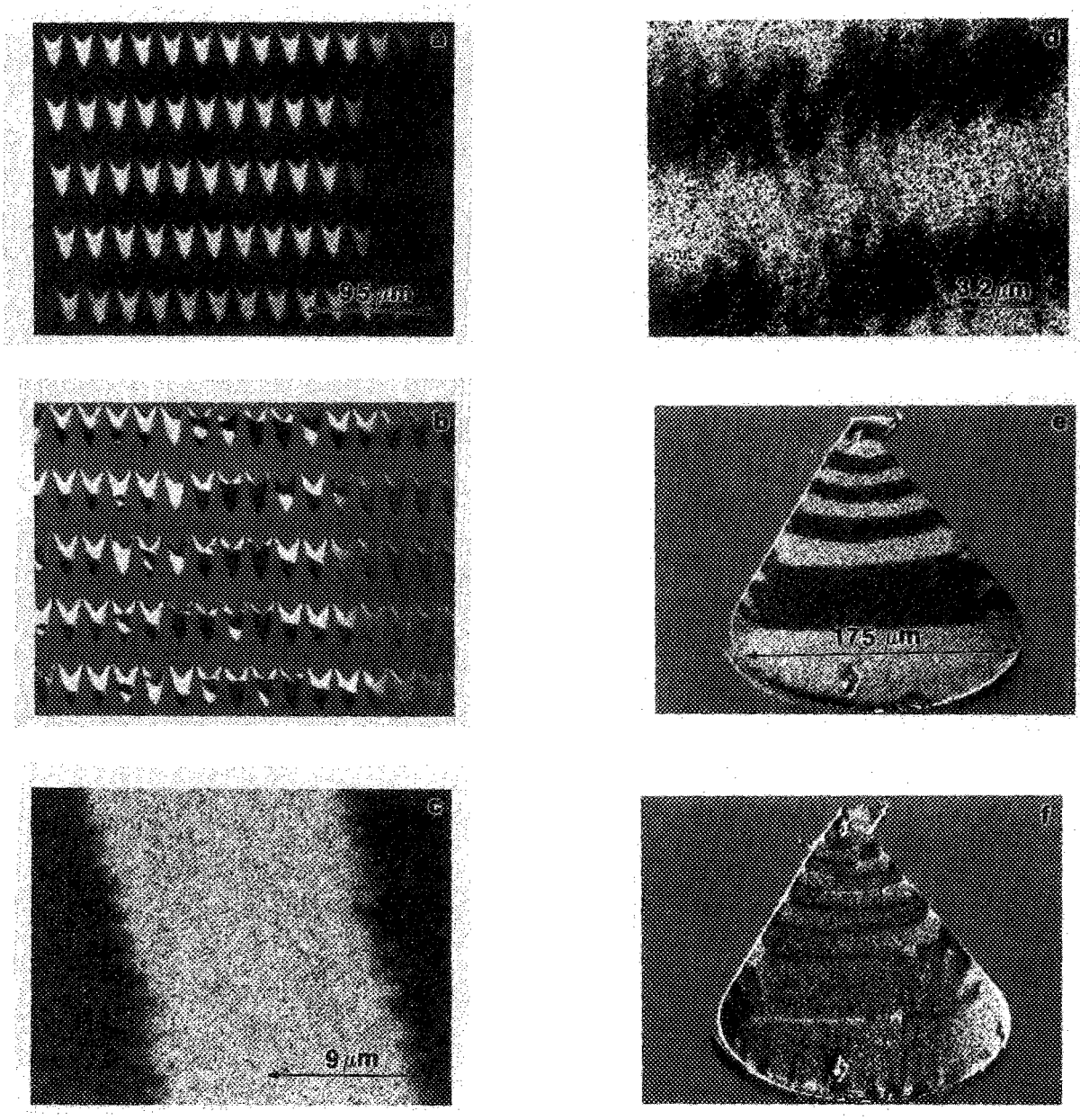

FIG. 15. (a) Auger map of Ni 54-eV line of magnetoresistive memory element array. Individual arrowheads are 15 μm across and 19 μm long. (b) M_x image corresponding to (a). (c) Low-density written bits on 700-Å CoNi, full scale width of 25 μm. (d) High-density written bits on 700-Å CoNi, full-scale width of 12.6 μm. (e) Thin-film magnetic recording head M_x and (f) M_y images. Head is approximately 175 μm wide.

magnetization of a permalloy thin-film recording head in Figs. 15(e) and 15(f), respectively. The permalloy is 1.5 μm thick. This sample was sputter cleaned with 1-keV Ar ions. The 256×192 images are 281 μm across. The dwell time per pixel is 10 ms. The domains in M_x and the closure domains in M_y are clearly visible. Defects in the preparation of magnetic thin films have been diagnosed in our lab using SEMPA.

ACKNOWLEDGMENTS

The iron whiskers were kindly furnished by A. Arrott of Simon Fraser University under an operating grant from the National Science and Engineering Research Council of Canada. The magnetoresisitive memory elements were supplied by D. Krahn of Honeywell. The magnetic recording heads were supplied by Control Data Corporation. Thanks to the accumulated efforts of all participating members of the Electron Physics Group. This work was supported in part by the Office of Naval Research.

LIST OF VARIABLES

E_0—Incident electron beam energy onto specimen.
I_0—Incident electron beam current onto specimen.
δ—Incident beam diameter on specimen.
W_d—SEM column objective lens working distance.
W_b—SEM column objective lens bore.

Θ_{st}—Specimen tilt angle relative to the incident beam.

Θ_{to}—Transport optics angle relative to plane perpendicular to the incident beam.

W_s—Distance from specimen to extraction electrode plane.

ΔE—Electron energy spread of electron source.

I_s—Emission current of electron source.

δ_s—Effective diameter of electron source.

P—Beam polarization; P_x, P_y, and P_z are components.

F—Electron spin analyzer figure of merit.

n—Normal to electron scattering plane.

$\mathbf{k}_i$—Electron wave-vector incident on scattering target.

$\mathbf{k}_f$—Electron wave-vector after scattering from scattering target.

$S(\Theta)$—Sherman function (spin-asymmetry scattering coefficient).

S—Detector Sherman function.

$\sigma(\Theta)$—Scattering cross section.

$I(\Theta)$—Angular intensity scattering in spin detector.

A—Scattering asymmetry.

N_L—Number of electrons scattered into left channel of spin detector.

N_R—Number of electrons scattered into right channel of spin detector.

A_I—Instrumental asymmetry.

A_{Id}—Displacement instrumental asymmetry.

$A_{I\Theta}$—Angular displacement asymmetry.

$d\sigma/d\Omega$—Differential scattering cross section.

$\Delta\Theta$—Angular tilt of incident beam in detector.

Δ—Displacement of incident beam in detector.

Θ_{in}—Inner detector angle relative to Au surface normal.

Θ_{out}—Outer detector angle relative to Au surface normal.

E_d,E_s—Energy of emitted secondaries in detector "d" and on the sample "s."

A_d,A_s—Illuminated area of emitted secondaries in detector "d" and on the sample "s."

Ω_d,Ω_s—Solid angle of emitted secondaries in detector "d" and on the sample "s."

V—SEMPA extraction electrode potential.

V_s—Emitted beam equivalent potential.

Θ_s—Angle of emitted secondary electrons relative to surface normal.

r_{max}—Maximum radius at extraction electrode of emitted secondaries.

Θ_f—Asymptotic angle of secondary electron trajectory at extraction electrode.

η_{exa}—Angular collection efficiency of extraction electrode which is the integral over E_s of a differential collection efficiency $d\eta_{exa}/dE_s$ multiplied by the electron energy distribution $N(E_s)$.

η_{exc}—Fraction (in energy) of secondary electrons collected by extraction optics.

δ_{se}—Secondary electron yield coefficient at specimen.

η_{to}—Transport efficiency of SEMPA optics.

η_{Au}—Collection yield in full detector.

η_{cp}—Channel plate collection efficiency.

η—Ratio of current on detector channel plate input to I_0.

E_i—Electrode potentials in transport and detector optics, $i = 1,2,\ldots$.

G_i—Grid electrode potentials in detector, $i = 1,2$.

D_i—Transport optics deflectors, $i = 1,2,\ldots$.

A_i—Transport optics apertures, $i = 1,2,\ldots$.

γ—Anode noise figure.

e—Electronic charge.

SNR—Signal-to-noise ratio.

τ—Dwell time per pixel during data acquisition.

n_v—Number of valence electrons/atom.

n_B—Number of Bohr magnetons/atom.

M—Sample magnetization; M_x, M_y, and M_z are components.

Θ—Magnetization angle in specimen plane.

W—Domain wall width on surface.

[1]F. Bitter, Phys. Rev. **38**, 1903 (1931).

[2]D. E. Newbury, D. E. Joy, P. Echlin, C. E. Fiori, and J. I. Goldstein, *Advanced Scanning Electron Microscopy and X-ray Microanalysis* (Plenum, New York, 1986).

[3]K. Tsuno, Rev. Solid State Sci. **2**, 623 (1988).

[4]J. P. Jacubovics, *Electron Microscopy in Materials Science Part IV*, edited by E. Ruedl and U. Valdre (Commission of European Communities, Brussels, 1973), p. 1305.

[5]J. N. Chapman, J. Phys. D **17**, 623 (1984).

[6]A. Wadas and P. Grutter, Phys. Rev. B **39**, 12013 (1989).

[7]J. Kranz and A. Z. Hubert, A. Agnew. Phys. **15**, 220 (1963).

[8]G. Chrobok and M. Hofmann, Phys. Lett. **57a**, 257 (1976).

[9]J. Unguris, D. T. Pierce, A. Galejs, and R. J. Celotta, Phys. Rev. Lett. **49**, 72 (1982).

[10]H. Hopster, R. Raue, E. Kisker, G. Guntherodt, and M. Campagna, Phys. Rev. Lett. **50**, 70 (1983).

[11]E. Kisker, W. Gudat, and K. Shroder, Solid State. Commun. **44**, 591 (1982).

[12]J. A. Venables, D. R. Batchelor, M. Hanbucken, C. J. Harland, and G. W. Jones, Philos. Trans. R. Soc. (London) A **318**, 243 (1986).

[13]K. Koike, H. Matsuyama, and K. Hayakawa, Scanning Microsc. Intern. Suppl. **1**, 241 (1987).

[14]J. Kirschner and H. P. Oepen, Phys. B1 **44**, 227 (1988).

[15]G. G. Hembree, J. Unguris, R. J. Celotta, and D. T. Pierce, Scanning Microsc. Intern. Suppl. **1**, 229 (1987).

[16]P. Morin, L. H. Ning, and F. Pellerin, Ultramicrosc. **28**, 103 (1989).

[17]J. I. Goldstein, D. E. Newbury, P. Echlin, D. C. Joy, C. Fiori, and E. Lifshin, *Scanning Electron Microscopy and X-Ray Microanalysis* (Plenum, New York, 1984).

[18]E. Munro and H. C. Chu, Optik **60**, 371 (1982).

[19]J. Orloff, Ultramicrosc. **28**, 88 (1989).

[20]C. A. Sanford and N. C. MacDonald, J. Vac. Sci. Technol. B **6**, 2005 (1988).

[21]M. Gesley, J. Vac. Sci. Technol. B **6**, 1984 (1988).

[22]D. W. Tuggle, J. Z. Li, and L. W. Swanson, J. Microsc. **140**, 293 (1985).

[23]J. Orloff, J. Microsc. **140**, 303 (1985).

[24]D. W. Tuggle and L. W. Swanson, J. Vac. Sci. Technol. B **3**, 193 (1985).

[25]P. W. Hawkes, *Magnetic Electron Lenses* (Springer, Heidelberg, 1982).

[26]J. A. Venables and A. P. Janssen, Ultramicrosc. **5**, 297 (1980).

[27]D. Penn, S. P. Apell, and S. M. Girvin, Phys. Rev. Lett. **55**, 518 (1985); J. Magn. Magn. Mater. **54–57**, 1041 (1986).

[28]L. Reimer, *Scanning Electron Microscopy* (Springer, Berlin, 1985).

[29]J. Kessler, *Polarized Electrons*, 2nd ed. (Springer, Berlin, 1985).

[30]M. Fink and A. C. Yates, At. Data **1**, 385 (1970).

[31]M. Fink and J. Ingram, At. Data **4**, 129 (1972).

[32]E. Kisker, R. Clauberg, and W. Gudat, Rev. Sci. Instrum. **53**, 1137 (1982).

[33]G. D. Fletcher, T. J. Gay, and M. S. Lubell, Phys. Rev. A **34**, 911 (1986).

[34]G. Holzwarth and H. J. Meister, Tables of Asymmetry Cross Sections

and Related Functions for Mott Scattering of Electrons by Screened Au and Hg Nuclei (University of Munich, Munich, 1964).
[35]M. Landolt, R. Allenspach, and D. Mauri, J. Appl. Phys. **57**, 3626 (1985).
[36]L. A. Hodge, T. J. Moravec, F. B. Dunning, and G. K. Walters, Rev. Sci. Instrum. **50**, 5 (1979).
[37]K. Jost, F. Kaussen, and J. Kessler, J. Phys. E **14**, 735 (1981).
[38]L. G. Gray, M. W. Hart, F. B. Dunning, and G. K. Walters, Rev. Sci. Instr. **55**, 88 (1984).
[39]D. M. Campbell, C. Hermann, G. Lampel, and R. Owens, J. Phys. E **18**, 664 (1985).
[40]F. B. Dunning, L. G. Gray, J. M. Ratliff, F.-C. Tang, X. Zhang, and G. K. Walters, Rev. Sci. Instrum. **58**, 1706 (1987).
[41]F.-C. Tang, X. Zhang, F. B. Dunning, and G. K. Walter, Rev. Sci. Instrum. **59**, 504 (1988).
[42]J. Kirschner and R. Feder, Phys. Rev. Lett. **42**, 1008 (1979).
[43]J. Kirschner and R. Feder, Surf. Sci. **104**, 448 (1981).
[44]J. Kirschner, *Polarized Electrons at Surfaces* (Springer, Berlin, 1985).
[45]J. Kirschner, Appl. Phys. A **36**, 121 (1985).
[46]H. C. Siegmann, D. T. Pierce, and R. J. Celotta, Phys. Rev. Lett. **46**, 452 (1981).
[47]R. J. Celotta, D. T. Pierce, H. C. Seigmann, and J. Unguris, Appl. Phys. Lett. **38**, 577 (1981).
[48]D. T. Pierce, S. M. Girvin, J. Unguris, and R. J. Celotta, Rev. Sci. Instrum. **52**, 1437 (1981).
[49]K. Koike, H. Matsuyama, and K. Hayakawa, Jpn. J. Appl. Phys. **27**(7), L1352 (1988).
[50]J. Unguris, D. T. Pierce, and R. J. Celotta, Rev. Sci. Instrum. **57**, 1314 (1986).
[51]D. T. Pierce, R. J. Celotta, M. H. Kelley, and J. Unguris, Nucl. Instrum. Methods A **266**, 550 (1988).
[52]M. R. Scheinfein, D. T. Pierce, J. Unguris, J. J. McClellend, and R. J. Celotta, Rev. Sci. Instrum. **60**, 1 (1989).
[53]J. Woods, M. Tobise, and R. C. O'Handley, Rev. Sci. Instrum. **60**, 688 (1989).
[54]J. Van Klinken, Nucl. Phys. **75**, 161 (1966).
[55]M. Uhrig, A. Beck, J. Goeke, F. Eschen, M. Sohn, G. F. Hanne, K. Jost, and J. Kessler, Rev. Sci. Instrum. **60**, 872 (1989).
[56]A. Gellrich, J. Jost, and J. Kessler, Proceedings of the 15th International Conference on the Physics of Electronic and Atomic Collisions (Brighton, U.K., 1987) ICPEAC-1987 (1987), p. 818.
[57]P. Grivet, *Electron Optics* (Pergamon Press, Oxford, 1965).
[58]P. A. Sturrock, *Static and Dynamic Electron Optics* (Cambridge University Press, New York, 1955).
[59]M. R. Scheinfein (unpublished).
[60]P. S. Farago, Adv. Elec. Phys. **21**, 1 (1965).
[61]R. E. Collins, J. Vac. Sci. Technol. **10**, 1106 (1973).
[62]S. S. Abhyankar and M. R. Bhiday, Proc. Indian Acad. Sci. A **74**, 53 (1971).
[63]M. J. M. Beerlage and P. S. Farago, J. Phys. E **14**, 928 (1981).
[64]M. R. Scheinfein, Optik **82**, 99 (1989).
[65]E. M. Purcell, Phys. Rev. **54**, 818 (1938).
[66]H. Wollnik, in *Focusing of Charged Particles*, edited by A. Septier (Academic, New York, 1967), Vol. 2.
[67]E. Harting and F. H. Read, *Electrostatic Lenses* (Elsevier Scientific, Amsterdam, 1976).
[68]M. R. Scheinfein and M. H. Kelley (unpublished).
[69]J. L. Wiza, Nucl. Instrum. Meth. **162**, 578 (1979).
[70]*Electronic Tubes*, Book 2, Part 3 (Mullard Ltd., Mullard House, Torrington Place, London, 1987), p. 400.
[71]H. Kersten, Ed., *Microchannel Plate Report* (FOM-Instituut voor Atoom-en Molecuulfysica, Amsterdam-Watergraafsmeer, 1982).
[72]E. H. Eberhardt, IEEE Trans. Nucl. Sci. **NS-28**, 712 (1981).
[73]E. H. Eberhardt, ITT Electro-Optical Prod. Div. Tech. Note 127 (1980).
[74]C. Loty, Acta Electron. **14**, 107 (1971).
[75]J. G. Timothy and R. L. Bybee, Rev. Sci. Instrum. **49**, 1192 (1978).
[76]Galileo model 3040, Galileo Electro-Optics Corp., Galileo Park, Sturbridge, MA 01518.
[77]L. J. Richter and W. Ho, Rev. Sci Instrum. **57**, 1469 (1986).
[78]Phillips Scientific, Mahwah, NJ.
[79]J. P. Boutot, J. C. Delmotte, J. A. Miehe, and B. Sipp, Rev. Sci. Instrum. **48**, 1405 (1977).
[80]L. Reimer, *Scanning Electron Microscopy* (Springer, Berlin, 1985), p. 155.
[81]W. Shockley and J. R. Pierce, Proc. Inst. Radio Eng. **26**, 321 (1938).
[82]R. Engstrom, RCA Photomultiplier Handbook, Appendix G (1980).
[83]B. Laprade and J. Cortez, Proc. SPIE **427**, 48 (1983).
[84]K. Eberhardt (private communication).
[85]K. Koike and K. Hayakawa, Jpn. J. Appl. Phys. **23**, L85 (1984).
[86]K. Koike and K Hayakawa, Jpn. J. Appl. Phys. **23**, L187 (1984).
[87]K. Koike and K. Hayakawa, Appl. Phys. Lett. **45**, 585 (1984).
[88]K. Koike, H. Matsuyama, H. Todokoro, and K. Hayakawa, Jpn. J. Appl. Phys. **24**, L542 (1985).
[89]K. Koike, H. Matsuyama, H. Todokoro, and K. Hayakawa, Jpn. J. Appl. Phys. **24**, 1078 (1985).
[90]K. Koike, H. Matsuyama, H. Todokoro and K. Hayakawa, Jpn. J. Appl. Phys. **24**, L833 (1985).
[91]K. Koike and K. Hayakawa, J. Appl. Phys. **57**, 4244 (1985).
[92]K. Koike and K. Hayakawa, IEEE Trans. J. Magn. Jpn. **TJMJ-1**, 486 (1985).
[93]H. Matsuyama, K. Koike, H. Todokoro, and K. Hayakawa, IEEE Transl. J. Magn. Jpn. **TJMJ-1**, 1071 (1985).
[94]K. Koike, H. Matsuyama, K. Mitsuoka, and K. Hayakawa, Jpn. J. Appl. Phys. **25**, L758 (1986).
[95]K. Koike and K. Hayakawa, in *Recent Magnetics for Electronics (1985/1986)*, edited by Y. Sakurai (Ohmsha Ltd., 1986) Vol. 21.
[96]K. Koike, H. Matsuyama, K. Hayakawa, K. Mitsuoka, S. Narishige, Y. Sugita, K. Shiiki, and C. Saka, Appl. Phys. Lett. **49**, 980 (1986).
[97]K. Mitsuoka, S. Sudo, N. Narishige, M. Hanazozo, Y. Sugita, K. Koike, H. Matsuyama, and K. Hayakawa, IEEE Trans. Magn. **MAG-23**, 2155 (1987).
[98]H. Matsuyama, K. Koike, K. Hayakawa, K. Mitsuoka, S. Sudo, S. Narishige, and Y. Sugita, IEEE Trans. Magn. **MAG-23**, 2173 (1987).
[99]K. Koike, H. Matsuyama, M. Todokoro, and K. Hayakawa, Scanning Microsc. **1**, 31 (1987).
[100]K. Hayakawa, K. Koike, and H. Matsuyama, Hitachi Inst. News **14**, 11 (1988).
[101]S. Suga and J. Kirschner, in *Physics of Magnetic Materials*, edited by M. Takahashi, S. Maekawa, Y. Gondo, and H. Nose (World Scientific, Singapore, 1987), p. 524.
[102]H. P. Oepen and J. Kirschner, Phys. Rev. Lett., **62**, 819 (1989).
[103]R. J. Celotta and D. T. Pierce, *Proceeding of Microbeam Analysis-1982*, edited by K.F. Heinrich (San Francisco Press, San Francisco, 1982), p. 469.
[104]J. Unguris, G. G. Hembree, R. J. Celotta, and D. T. Pierce, J. Microsc. **139**, RP1 (1985).
[105]A. L. Robinson, Science **230**, 53 (1985).
[106]G. G. Hembree, J. Unguris, R. J. Celotta, and D. T. Pierce, *Proceedings of the 44th EMSA Meeting*, edited by G. W. Bailey (San Francisco Press, San Francisco, 1986), p. 634.
[107]J. Unguris, G. G. Hembree, R. J. Celotta, and D. T. Pierce, J. Magn. Magn. Mater. **54-57**, 1629 (1986).
[108]R. J. Celotta and D. T. Pierce, Science **234**, 249 (1986).
[109]J. Unguris, G. G. Hembree, R. J. Celotta, and D. T. Pierce, J. Vac. Sci. Technol. A **5**, 1976 (1987).
[110]R. J. Celotta, J. Unguris, and D. T. Pierce, J. Vac. Sci. Technol. A **6**, 574 (1988).
[111]R. J. Celotta, Appl. Surf. Sci. **31**, 59 (1988).
[112]D. T. Pierce, J. Unguris, and R. J. Celotta, MRS Techn. Bull. **XIII**, 19 (1988).
[113]D. T. Pierce, Phys. Scripta **38**, 291 (1988).
[114]M. H. Kelley, J. Unguris, M. R. Scheinfein, D. T. Pierce, and R. J. Celotta, *Proceedings of the Microbeam Analysis Society - 1989*, edited by P. E. Russell (San Francisco Press, San Francisco, 1989), p. 391.
[115]J. Unguris, M. R. Scheinfein, R. J. Celotta, and D. T. Pierce, IEEE Trans. Magn. **MAG-25**, 4204 (1989).
[116]M. R. Scheinfein, D. T Pierce, J. Unguris, and R. J. Celotta, in *Magnetic Properties in Low Dimensional Systems-II*, edited by L. Falicov and J. L Moran-Lopez (Springer, Berlin, 1990), p. 2.
[117]M. R. Scheinfein, J. Unguris, D. T. Pierce, and R. J. Celotta, Phys. Rev. Lett. **63**, 668 (1989).
[118]J. Unguris, M. R. Scheinfein, D. T. Pierce, and R. J. Celotta, Appl. Phys. Lett. **55**, 2553 (1989).
[119]M. Aeschlimann, M. R. Scheinfein, J. Unguris, F. J. A. M. Greidanus, and S. Klahn (to be published).
[120]A. Hubert (private communication).